Check for updates

Journal of
**Materials Chemistry A**

Materials for energy and sustainability

rsc.li/materials-a

Volume 6
Number 12
28 March 2018
Pages 4883-5230

ISSN 2050-7488

ROYAL SOCIETY
OF CHEMISTRY

COMMUNICATION
Zhenhai Wen et al.
An electrochemically neutralized energy-assisted low-cost acid-alkaline electrolyzer for energy-saving electrolysis hydrogen generation

This is an Accepted Manuscript, which has been through the Royal Society of Chemistry peer review process and has been accepted for publication.

Accepted Manuscripts are published online shortly after acceptance, before technical editing, formatting and proof reading. Using this free service, authors can make their results available to the community, in citable form, before we publish the edited article. We will replace this Accepted Manuscript with the edited and formatted Advance Article as soon as it is available.

You can find more information about Accepted Manuscripts in the Information for Authors.

Please note that technical editing may introduce minor changes to the text and/or graphics, which may alter content. The journal's standard Terms & Conditions and the Ethical guidelines still apply. In no event shall the Royal Society of Chemistry be held responsible for any errors or omissions in this Accepted Manuscript or any consequences arising from the use of any information it contains.

ROYAL SOCIETY
OF CHEMISTRY

rsc.li/materials-a

# ARTICLE

# Metal-Organic Frameworks and Their derivatives for Electrochemical CO$_2$ Reduction Reaction: Insights from Molecular Engineering

Xiaoming Liu,[a] Xuan-He Liu, *[a] Xiangrui Zhang,[a] Huan Wang,[b] and Qinglan Zhao [c]*

Excessive fossil fuel consumption has led to a rapid increase in CO$_2$ concentration, posing a threat to the global environment. The electrochemical conversion of CO$_2$ back into valuable carbon-containing products offers a promising solution, however the lack of efficient electrocatalysts remains a challenge for high-efficiency CO$_2$ reduction reaction (CO$_2$RR). Metal-organic frameworks (MOFs) have emerged as promising electrocatalysts owing to their superior activity and well-defined active sites, which are recognized as model electrocatalysts for fundamental study of the electrocatalytic reaction mechanisms. In this review, focusing on the roles of metal and coordination environment, we have discussed the molecular engineering of MOF electrocatalysts for CO$_2$RR, including regulation of metal nodes, modulation of surrounding organic ligands, and post-modification of MOFs. In addition, stability of MOFs and transformation strategies through wet chemistry method and pyrolysis treatment to obtain MOF derivatives are summarized. The metal centers, coordination environment of N atoms and other heteroatoms of the MOF derivatives are discussed for their performance in CO$_2$RR. Furthermore, computational simulations and advanced characterizations are also summarized to understand the correlation of structure and performance for MOFs and their derivatives. By overviewing the progress and current challenges of the MOF electrocatalysts and their derivatives for CO$_2$RR, we are aiming to provide insights into design principles and propose future directions for high-efficiency electrocatalysts, paving the way toward carbon neutrality.

## 1. Introduction

Since the industrial revolution, there has been a dramatic increase in human demand for energy[1], leading to a great energy crisis. Furthermore, the excessive consumption of fossil fuels such as coal, oil and natural gas has resulted in a rapid increase in global concentration of CO$_2$ and related environmental issues[2]. For example, the high concentration of greenhouse gases reduces the infrared radiation emitted into space, leading to the warming earth, melting glaciers, and ultimately the rise in sea levels[3]. As a result, the concept of carbon neutrality was proposed by the Paris Agreement[4], to bring converting the released CO$_2$ back to carbon products to achieve net zero emission by 2050.

In recent decades, tremendous efforts have been dedicated to CO$_2$ conversion with various strategies including photochemical[5], thermochemical[6], biochemical[7, 8], chemical reforming[9-11], mineralization[12], electrochemical[13-15] methods, and so on. Among these, electrochemical CO$_2$ reduction

reaction (CO$_2$RR) stands out as a promising approach to achieving carbon neutrality, as it can be conducted in mild aqueous solution conditions with the input of renewable electricity[16, 17]. In this regard, numerous constructive research studies have been reported to achieve high-performance electrocatalytic CO$_2$RR toward formation of valuable reduced carbon products, by enhancing selectivity[18, 19], energy efficiency[20, 21], and stability[22, 23]. In the past few years, significant efforts have been devoted to developing efficient electrocatalysts for CO$_2$RR, such as metal nanoparticles (e. g., Ag, Au, Cu, Zn and Sn)[24-29], metal complexes (e. g., oxides, sulfides and nitrides) [30-32], carbonaceous materials[33], and metal-organic frameworks[34, 35].

Metal-organic frameworks (MOFs), a type of crystalline porous materials with periodic network structure formed by the self-assembly of transition metal ions and organic ligands, have been intensively studied as electrocatalysts for CO$_2$RR[36, 37] due to their large specific surface area, tunable structure and ordered structure[38]. Furthermore, their well-defined structures and uniform active centers make it easy to construct reliable structural models to understand the mechanism of CO$_2$RR[39, 40]. It has been reported that both metal species[41, 42] and organic linkers[43, 44] of MOFs can serve as active sites or modifiers to drive electrocatalytic reactions. Besides MOFs, MOF-derived electrocatalysts, especially those with precisely active centers, also play a crucial role in influencing the CO$_2$RR activity and selectivity through the manipulation of the electronic structure[45-48].

[a.] School of Science, China University of Geosciences (Beijing), Beijing 100083, China.
[b.] Key Laboratory of Advanced Energy Materials Chemistry (Ministry of Education), Nankai University, Tianjin 300071, China.
[c.] Department of Chemical and Biological Engineering, The Hong Kong University of Science and Technology, Clear Water Bay, Kowloon, Hong Kong, China.
† Footnotes relating to the title and/or authors should appear here.
Electronic Supplementary Information (ESI) available: [details of any supplementary information available should be included here]. See DOI: 10.1039/x0xx00000x
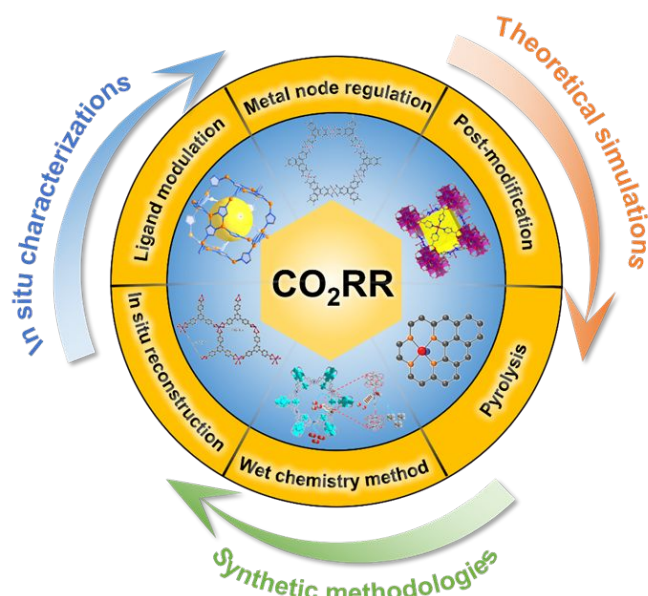
**Fig. 1** Scheme of molecular engineering strategy including regulation of metal nodes, modulation of surrounding organic ligands and post-modification of MOFs; *in situ* characterization and reconstruction; wet chemistry method and pyrolysis treatment for MOF derivatives for $CO_2RR$. (Molecular structures shown in the scheme have been cited from references [53-58] with copyright approval from Wiley-VCH and American Chemical Society.)

Based on the understanding of the roles of active metal nodes and coordinating organic ligands of MOF electrocatalysts, we discuss the molecular engineering strategy including regulation of metal nodes, modulation of surrounding organic ligands, and post-modification of MOFs for $CO_2RR$ (**Fig. 1**). Regarding the MOF derivatives, we discuss transformation strategies including wet chemistry method at mild temperature and pyrolysis treatment at high temperature. In particular, the significant impacts of metal centers and coordination environment surrounded by N atoms and other heteroatoms on performance of $CO_2RR$ are discussed. Advanced structural characterizations combined with the first-principle density functional theory (DFT) calculations to unravel the active sites for MOFs at atomic and molecular level are summarized to help understand the relationship between structure and performance[49-52]. Finally, the current challenges and future directions are proposed for advancing MOF-based electrocatalysts for $CO_2RR$.

## 2. Fundamentals of $CO_2$ Reduction Reaction

The $\sigma$ and $\pi_3^4$ bonds of linear $CO_2$ molecule rendering the C=O bond a certain degree of triple-bond character, which is thermodynamically stable and chemically inert[3]. Therefore, $CO_2RR$ is typically kinetically sluggish[59], especially toward high-energy and value-added carbon products formation with multi-proton and multi-electron transfer steps, such as $CH_4$ (8e$^-$), $CH_3OH$ (6e$^-$), $C_2H_4$ (12e$^-$), and $C_2H_5OH$ (12e$^-$)[60]. Up to now, at

**Table 1** The half reactions of $CO_2RR$ and corresponding equilibrium potentials at pH of 6.8 *vs.* RHE calculated from tabulated thermodynamic data in aqueous solution.

| Half reactions | Equilibrium potentials (*vs.* RHE) | Number |
|---|---|---|
| $CO_2 + 2H^+ + 2e^- \rightarrow HCOOH$ (aq) | $E^0 = -0.02$ V | (1) |
| $CO_2 + 2H^+ + 2e^- \rightarrow CO$ (g) $+H_2O$ (l) | $E^0 = -0.10$ V | (2) |
| $CO_2 + 8H^+ + 8e^- \rightarrow CH_4$ (g) $+ 2H_2O$ (l) | $E^0 = 0.17$ V | (3) |
| $CO_2 + 4H^+ + 4e^- \rightarrow HCHO$ (aq) $+ H_2O$ (l) | $E^0 = -1.31$ V | (4) |
| $CO_2 + 4H^+ + 4e^- \rightarrow C$ (s) $+ H_2O$ (l) | $E^0 = 0.21$ V | (5) |
| $CO_2 + 6H^+ + 6e^- \rightarrow CH_3OH$ (aq) $+H_2O$ (l) | $E^0 = 0.03$ V | (6) |
| $2CO_2 + 12H^+ + 12e^- \rightarrow C_2H_4$ (g) $+ 4H_2O$ (l) | $E^0 = 0.08$ V | (7) |
| $2CO_2 + 12H^+ + 12e^- \rightarrow C_2H_5OH$ (aq) $+ 3H_2O$ (l) | $E^0 = 0.09$ V | (8) |
| $2CO_2 + 8H^+ + 8e^- \rightarrow CH_3COOH$ (aq) $+ 2H_2O$ (l) | $E^0 = -0.26$ V | (9) |
| $2CO_2 + 10H^+ + 10e^- \rightarrow CH_3CHO$ (aq) $+ 3H_2O$ (l) | $E^0 = 0.05$ V | (10) |
| $2CO_2 + 14H^+ + 14e^- \rightarrow C_2H_6$ (aq) $+ 4H_2O$ (l) | $E^0 = 0.14$ V | (11) |
| $2CO_2 + 2H^+ + 2e^- \rightarrow H_2C_2O_4$ (aq) | $E^0 = -0.91$ V | (12) |
| $2CO_2 + 16H^+ + 16e^- \rightarrow C_2H_5CHO$ (aq) $+ 5H_2O$ (l) | $E^0 = 0.14$ V | (13) |
| $3CO_2 + 18H^+ + 18e^- \rightarrow C_2H_5CH_2OH$ (aq) $+ 5H_2O$ (l) | $E^0 = 0.21$ V | (14) |
| $3CO_2 + 20H^+ + 20e^- \rightarrow C_3H_8$ (g) $+ 6H_2O$ (l) | $E^0 = 0.09$ V | (15) |
| $3CO_2 + 16H^+ + 16e^- \rightarrow (CH_3)_2CO$ (aq) $+ 5H_2O$ (l) | $E^0 = -0.26$ V | (16) |
| $2H^+ + 2e^- \rightarrow H_2$ (g) | $E^0 = 0$ V | (17) |

least 16 products have been identified in $CO_2RR$, with their corresponding half reactions listed in **Table 1**[61-63], leading to the occurrence of complex reactions yielding various carbon products. Moreover, the hydrogen evolution reaction (HER) with an equilibrium potential of 0 V *vs.* reversible hydrogen electrode (RHE) hinders $CO_2RR$ as a competition reaction. Therefore, it is a significant challenge to achieve certain desired reduction products with high selectivity and activity.

As summarized in **Table 2**, CO and HCOOH in 2-electron transfer reactions are common reduction products, whose Faradaic efficiencies (FEs) reach up to 100% in the MOF-based catalysts[54, 64-66]. However, FEs usually drop when multiple steps with more electrons are involved in the reaction system. For example, $CH_4$, an 8-electron transfer product, needs a complex multiple proton-coupled electron transfer (PCET) process, which has lower selectivity of $CO_2$-to-$CH_4$ electroreduction[67, 68]. At this stage, the reported FEs for $CH_4$ can reach 92% on [$Cu_4ZnCl_4$(btdd)$_3$] ($Cu_4$-MFU-4*l*, $H_2$btdd = bis(1*H*-1,2,3-triazolo-[4,5-*b*],[4',5'-*i*])dibenzo-[1,4]-dioxin) with trigonal pyramidal Cu(I)N$_3$ active sites[69]. $C_2H_4$ and $C_2H_5OH$, 12-electron transfer

Table 2 Summary of CO2RR products over recently reported MOFs-based electrocatalysts.

| Sample | Main product | FE (%) | Potential (vs. RHE) | Stability (h) | Ref. |
|---|---|---|---|---|---|
| Ag@UiO-66-SH | CO | 74.0 | -1.10 | 10 | [74] |
| $Fe_2$-$N_6$-C-$o$ | CO | >80.0 | -0.5 to -0.9 | 21 | [75] |
| ZIF-8 | CO | 81.0 | -1.10 | — | [76] |
| CoPc-Cu-O | CO | 85.0 | -0.63 | 10 | [77] |
| $PcCu$-$O_8$-Zn | CO | 88.0 | -0.70 | > 10 | [78] |
| $Cu_{0.5}Zn_{0.5}$/ZIF-8 | CO | 88.5 | -1.00 | > 6 | [79] |
| Fe@BIF-73-NS | CO | 88.6 | -1.8 V vs. Ag/AgCl | 14 | [80] |
| ZIF-A-LD | CO | 90.57 | -1.10 | 10 | [81] |
| Zr-BTB@Hemin-TMA | CO | 92.0 | -1.20 | 3.0 | [82] |
| Ga-$N_3$S-PC | CO | 92.0 | -0.30 | 24 | [83] |
| NCMSH | CO | 92.68 | -0.70 | > 24 | [84] |
| Fe-$N_{2+2}$-$C_8$ | CO | 93.0 | -0.47 | 20 | [85] |
| Fe-$N_5$/DPCF | CO | 93.1 | -0.50 | 25 | [86] |
| Ag/Zr-$fcu$-MOF-NDC | CO | 94.0 | -1.00 | 1 | [87] |
| CALF20 | CO | 94.5 | -0.97 | ~2.2 | [88] |
| Co-$N_2$ | CO | 95.0 | -0.68 | 60 | [89] |
| O-Fe-N-C | CO | 95.0 | -0.50 | 30 | [58] |
| Ni-SNC | CO | 95.0 | -0.80 | 24 | [90] |
| Bi-BTC-D | CO | 95.5 | -0.86 | 12 | [65] |
| Ni-$N_3$-C | CO | 95.6 | -0.65 | 10 | [48] |
| 1-$NH_2$ | CO | 96.0 | -2.30 | 300 | [91] |
| $CuN_3O$/C | CO | 96.0 | -0.80 | 15 | [92] |
| $Fe_1$-$Ni_1$-N-C | CO | 96.2 | -0.50 | 10 | [46] |
| $CoCp_2$@MOF-545-Co | CO | 97.0 | -0.70 | 8 | [93] |
| Ni/HNC | CO | 97.2 | -0.70 | 10 | [94] |
| ZIF-NC-Ni-Fe | CO | 97.8 | -0.60 | 50 | [95] |
| NiSA-$N_2$-C | CO | 98.0 | -0.80 | 10 | [34] |
| Cu-Fe-$N_6$-C | CO | 98.0 | -0.70 | 10 | [96] |
| S/Fe-po$N_4$-C | CO | 98.2 | -0.58 | >12 | [97] |
| MOF Ni-Fe | CO | 98.2 | -0.50 | 30 | [54] |
| Ni SAC-1000 | CO | 98.24 | -0.80 | 24 | [98] |
| NiPc-$NiO_4$ | CO | 98.4 | -0.85 | 10 | [66] |
| K-defect-C-1100 | CO | 99.0 | -0.45 | 10 | [99] |
| Fe/Cu-N-C | CO | ~99.0 | -0.80 | 60 | [100] |
| Fe-$S_1N_3$ | CO | 99.02 | -0.50 | 40 | [47] |
| Ni/Cu-N-C | CO | 99.2 | -0.79 | 60 | [101] |
| FeTCPP⊂UiO-66 | CO | ~100 | -0.56 | 2.5 | [102] |
| H-3DOM-$ZnN_4$/P-C | CO | ~100 | -0.60 | >30 | [103] |
| $ZnN_4S_1$/P-HC | CO | ~100 | -0.60 | >30 | [104] |
| Bi/UiO-66 | HCOOH | 70~85 | -0.4 to -0.7 | 1.1 | [105] |
| In-BDC | $HCOO^-$ | 88.0 | -0.669 | 21 | [106] |
| $Me_2NH_2^+${$In^{III}$-[Ni$(C_2S_2(C_6H_4COO)_2)_2$]}·3DMF·1.5$H_2O$ | $HCOO^-$ | 89.6 | -1.30 | 12 | [107] |
| Bi-HHTP | HCOOH | 90.0% | 2.60 | >30 | [108] |
| FJU-127-$CH_3$ | $HCOO^-$ | 90.2 | -1.57 | 5 | [109] |
| Bi-ZMOF | HCOOH | 91.0 | -1.10 | 12 | [110] |
| BiZn-MOF | $HCOO^-$ | 92.0 | -0.90 | 13 | [111] |
| Bi NS | $HCOO^-$ | 92.0 | -1.10 | 10 | [112] |
| $Sb_{2.5}$/Bi@C | HCOOH | 94.8 | -1.40 | 30 | [113] |
| Bi(btb) | $HCOO^-$ | 95.0 | -0.97 | 32 | [56] |
| Bi-HHTP | $HCOO^-$ | > 95.0 | -0.70 | >30 | [114] |

*Journal of Materials Chemistry A Accepted Manuscript*

**ARTICLE**

| | | | | | |
|---|---|---|---|---|---|
| CAU-17 MOFs | HCOOH | 95.5 | -1.10 | 10 | [115] |
| Bi-BTC | HCOO$^-$ | 96.0 | -0.90 | 24 | [116] |
| Ce$_2$-Bi@C | HCOO$^-$ | 97.2 | -1.10 | 48 | [117] |
| In$_2$O$_{3-x}$@C | HCOOH | 98.0 | -1.20 | 120 | [64] |
| Bi-ene | HCOO$^-$ | ~100 | -0.8 to -1.2 | 12 | [118] |
| Cu-PorOH | CH$_4$ | 51.3 | -1.50 | 6 | [67] |
| Cu/a-C | CH$_4$ | 55.0 | -1.40 | 12.5 | [119] |
| Cu-DBC | CH$_4$ | 56.0 | -1.40 | 4 | [120] |
| Cu-I | CH$_4$ | 57.2 | -1.08 | 10 | [52] |
| Cu$_2$O@Cu-MOF | CH$_4$ | 63.2 | -1.71 | 1 | [121] |
| 2D-vc-MOF(Cu) | CH$_4$ | 65.0 | -1.40 | 4 | [122] |
| MCH-3 | CH$_4$ | 76.7 | -1.00 | 100 min | [123] |
| HATNA-Cu-MOF | CH$_4$ | 78.0 | -1.50 | 12 | [124] |
| Cu/CeO$_2$@C | CH$_4$ | 80.3 | -1.50 | 9 | [125] |
| 2Bn-Cu@ UiO-67 | CH$_4$ | 81.0 | -1.50 | 6 min | [126] |
| Cu$_4$-MFU-4/ | CH$_4$ | 92.0 | -1.20 | 24 | [69] |
| BIF-102NSs | C$_2$H$_4$ | 11.3 | -1.00 | 5 | [127] |
| Fe-TCPP@Cu | C$_2$H$_4$ | 33.42 | -1.17 | 5 | [128] |
| CuN$_2$/Cu(111) | C$_2$H$_4$ | 41.5 | — | 6 | [129] |
| Cu-MOF-CF | C$_2$H$_4$ | 48.6 | -1.10 | 12 | [73] |
| C/HKUST-1/Cu/PTFE | C$_2$H$_4$ | 54.0 | -4.00 | 65 | [71] |
| PcCu-Cu-O | C$_2$H$_4$ | 50.0 | -1.20 | 4 | [72] |
| Cutrz | C$_2$H$_4$ | 50.0 | -1.20 | 80 | [130] |
| Cu-HITP@PDA | C$_2$H$_4$ | 51.0 | -1.20 | 10 | [131] |
| MAF-2E，MAF-2E MAF-2P | C$_2$H$_4$ | 51.2±2.3 | -1.10--1.50 | 10 | [53] |
| CuTrz-109 | C$_2$H$_4$ | 55.4 | -1.15 | 10 | [132] |
| Ag/Cu/Cu$_2$OAg$_{0.1}$/HKUST-1 | C$_2$H$_4$ | 57.2 | -1.30 | 10 | [133] |
| S-HKUST-1 | C$_2$H$_4$ | 60.0±2.0 | -1.32 | 8 | [134] |
| KB@Cu$_3$(HITP)$_2$ | C$_2$H$_4$ | 70.0 | -1.37 | 10 | [135] |
| Cu-SAs@Ir-PCN-222-PA | C$_2$H$_4$ | 70.9 | -1.00 | 16 | [57] |
| CuPz$_2$-Act-30 | C$_2$H$_4$ | 70.2±1.7 | -1.03 | 12 | [136] |
| Cu-Cu$_2$O@CC | CH$_3$OH | 37.4 | -0.70 | 6 | [137] |
| OD-Cu/C | CH$_3$OH | ~43.2 | -0.30 | 15 | [138] |
| Cu@Cu$_2$O-400 °C | CH$_3$OH | 45.0 | -0.70 | 10 | [139] |
| Cu$_3$(HHTQ)$_2$ | CH$_3$OH | 53.6 | -0.40 | 10 | [140] |
| CuNi SAs/UiO-66(Hf) | CH$_3$OH | ~98.0 | — | — | [141] |
| Cutrz | CH$_3$COOH | 2.20 | -1.20 | 80 | [130] |
| CuN$_2$/Cu(111) | C$_2$H$_5$OH | 18.2 | — | 6 | [129] |
| Cutrz | C$_2$H$_5$OH | 19.7 | -1.20 | 80 | [130] |
| Cu-MMT-H$_2$O | C$_2$H$_5$OH | 20.8 | -1.15 | — | [142] |
| Cu$_{2-x}$Se-450 | C$_2$H$_5$OH | 42.0 | -0.74 | — | [143] |
| CuAg$_5$@NC | C$_2$H$_5$OH | 51.8 | -1.00 | 20 | [144] |
| CuSn-HAB | C$_2$H$_5$OH | 56.0 | -0.57 | 65 | [145] |
| OM-Cu-NiSNC | C$_2$H$_5$OH | 63.0 | -0.76 | 50 | [146] |
| Cu GNC-VL | C$_2$H$_5$OH | 70.52 | -0.87 | 12 | [147] |
| Cu$_2$N$_4$/Cu(111) | n-C$_3$H$_7$OH | 3.40 | — | 6 | [129] |
| CuN$_2$/Cu(111) | n-C$_3$H$_7$OH | 5.10 | — | 6 | [129] |
| Cu-SA/NPC | CH$_3$COCH$_3$ | 36.70 | -0.36 | 10 | [148] |
| Cu$_{0.85}$Zn$_{0.15}$/C | CH$_3$COCH$_3$ | 38.10 | -0.40 | — | [149] |

products, exhibit even more descending FEs (mostly below 60%) on the MOF-based catalysts[70-73].

    **Fig. 2** shows the possible intricate pathways of CO$_2$RR classified by various reduction products. Variations in the final products – such as CO, CH$_4$, CH$_3$OH, C$_2$H$_4$, C$_2$H$_5$OH and so on can happen on the electrocatalysts with the same or different metal surfaces. For example, CO is a common product obtained on metals including Cu, Au, Ni, and Co during the electrocatalytic process.[150-153] Furthermore, differences in facets, sizes, and oxidation states of Cu can lead to various products [154-156] such as CO, CH$_3$OH and C$_2$H$_4$. Another example is formate, which is mostly produced on Bi and sometimes on In and Sb catalysts[64, 106, 157]. Here, the possible reaction pathways are categorized by various reduction products, as shown in **Fig. 2**. In CO$_2$RR, *H,
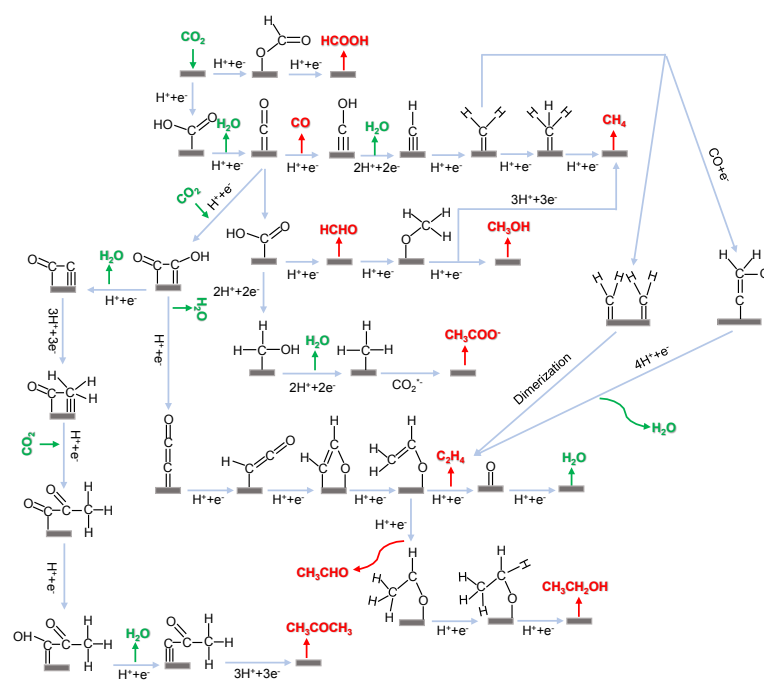
**Fig. 2** Possible pathways of $CO_2RR$ toward various reduction products.

*CO, and *COOH (* denotes the surface-bond site) are typically key intermediates[158] that can further convert into various reaction intermediates. *H is involved in the PCET process in the reduction pathways. *CO is a common intermediate for forming deeply reduced products. The electrophilicity of C and O in *CO dictates the subsequent reduction pathways. When O atom in *CO first accepts a proton to generate *COH, it undergoes further reduction by accepting multiple protons and losing one water molecule to generate $CH_4$. On the other hand, when C atom first accepts a proton to generate *CHO, the double bond between C and O opens to generate *CHOH, and further hydrogenation on C to produce methanol. Similar cases are also applied for *COOH and *HCOO. In terms of *COOH intermediate, it is formed by transferring proton to O atom of $CO_2$, followed by removing one water molecule to generate *CO. As for *HCOO, it is formed by transferring proton to the C atom of $CO_2$, followed by further hydrogenation to produce formate.

## 3. Electrochemical Measurements and Performance Assessments

Evaluating the performance of the electrocatalysts is crucial and is typically conducted using an electrochemical three-electrode system. Commonly employed testing techniques, including chronoamperometry/chronovoltammetry, linear sweep voltammetry (LSV), and electrochemical impedance spectroscopy (EIS) are utilized to determine parameters such as Faraday efficiency (FE), current density (J), overpotential (η), Tafel slope (*b*), turnover frequency (TOF), electrochemical surface area (ECSA) and stability. The key electrochemical characterization methods and evaluation parameters for electrocatalysts are summarized below.

### 3.1 Electrochemical measurements

#### 3.1.1 Chronoamperometry/Chronovoltammetry

Chronoamperometry is an electrochemical analysis technique that involves applying a constant potential step to the working electrode of an electrochemical system, and tracking the current response over time. On the other hand, Chronovoltammetry applies a rapidly rising pulse current to the working electrode of an electrolytic cell, measuring the voltage between the working electrode and the reference electrode as a function of time. Both two techniques are commonly used methods for the performance evaluation of $CO_2RR$, from which Faradaic efficiency, (partial) current density, and stability can be obtained.

#### 3.1.2 Linear sweep voltammetry (LSV)

LSV involves applying a linearly changing scanning potential and recording the corresponded current. The LSV curve is essentially half of a CV curve. In a reversible reaction, the peak current increases with the number of electrons gained or lost and the reaction area. The scanning speed directly affects the thickness of the diffusion layer. Higher scanning speed result in thinner diffusion layer, greater potential gradient, and greater current. Therefore, the scanning speed needs to be controlled during testing. Additionally, LSV can be also transformed to obtain a Tafel plot, providing insights into the reaction mechanism.

#### 3.1.3 Electrochemical impedance spectroscopy (EIS)

EIS entails the application of a small amplitude alternating current potential wave with varying frequencies to an electrochemical system. By measuring the ratio of the alternating current potential to the current signal versus the sine wave frequency (ω), or the change in the impedance phase

angle ($\Phi$) with frequency, EIS offers valuable information about the system. As conductivity of MOFs is still one of the challenges to be addressed when applied as electrocatalysts for $CO_2RR$, EIS can be an effective method to evaluate the feasibility of MOF catalysts from the evaluation of resistance.

## 3.2 Performance assessments

### 3.2.1 Faradaic efficiency (FE)

FE is a crucial parameter for evaluating the selectivity of electrocatalysts. It is defined as the percentage of charge consumed to generate the desired products in the total charge during the $CO_2RR$ process[159], which can be expressed as:

$$FE = \frac{\alpha n F}{Q} * 100\%$$

(18)

where $\alpha$ is the molar amount of the desired product; $n$ is the number of electrons transferred to obtain a certain product; F is the Faraday constant (96485 C/mol); Q is the total charge consumed in the entire reaction.

### 3.2.2 Current density (J)

$J$ reflects the reaction efficiency of the electrochemical conversion, usually including the total current density ($J_t$) and partial current density ($J_p$). $J_t$ can be calculated by dividing the total current by the geometric area of the working electrode (S). $J_p$ is obtained by multiplying the FE with $J_t$, which corresponds to the production rates of a certain product:

$$J_t = J/S \quad (19)$$
$$J_p = FE \times J_t$$

(20)

### 3.2.3 Overpotential (η)

$\eta$ is a criterion for assessing the activity of electrocatalysts, representing the additional driving force required to overcome the reaction energy barrier and facilitate the redox reaction. It can be described as the difference between the standard thermodynamic reaction potential ($E^0$) and the practical electrode potential ($E_{cat}$)[160], as shown in the following equation:

$$\eta = E^0 - E_{cat} \quad (21)$$

### 3.2.4 Tafel slope (b)

Tafel slope reflects the kinetics of electrocatalysts for $CO_2RR$. A smaller Tafel slope indicates faster kinetics and superior performance. The Tafel slope is related to the overpotential, which can be calculated according to the following equation:

$$\eta = b*logj_p + a \quad (22)$$

Here, $\eta$, $b$, $j_p$, and $a$ represent the overpotential, Tafel slope, partial current density of a certain product, and a constant. When the Tafel slope is close to 118 mV·dec$^{-1}$ or 59 mV·dec$^{-1}$, the reaction rate is determined by the $CO_2$ activation or the *COOH intermediate formation [161].

### 3.2.5 Turnover frequency (TOF)

TOF, defined as the total number of molecules that undergo reaction per second per active site, usually reflect the intrinsic activity of an individual active site of catalysts[162]. TOF can be calculate by:

$$TOF = (J_t \times FE)/(nFn_a) \quad$$

(23)

where $J_t$, FE, $n$, $F$ and $n_a$ represent the total current density, Faraday efficiency, electron transfer number for a desired product, Faraday constant (96485 C/mol) and the number of active sites on the electrode.

### 3.2.6 Electrochemical surface area (ECSA)

The total current density, calculated with respect to the geometric area of the electrode, is indicative of the catalyst loading and specific surface area, a metric that can be normalized through ECSA. A greater ECSA value typically correlates with enhanced $CO_2$ reduction performance. The ECSA can be approximated using the double-layer capacitance ($C_{dl}$):

$$ECSA = C_{dl}/C_s \quad (24)$$

in which $C_{dl}$ is obtained by measuring the current with different scanning rates at a nonfaraday current area and $C_s$ is the specific capacitance of smooth surface samples.

### 3.2.7 Stability

Stability is a crucial evaluation criterion for practical application. The long-term stability can be evaluated by chronoamperometry and chronovoltammetry. The greater stability is denoted by minimal fluctuation during testing. At this stage, stability remains one of the bottlenecks of MOFs electrocatalysts, which will be discussed later in this review.

## 4. Insights into Catalyst Design: Why MOFs?

As discussed, there are so many possible pathways toward various products occur during $CO_2RR$. Developing high-selectivity electrocatalysts is still a great challenge in this field. A deep insight into the structure-reactivity correlations is thus highly demanded to provide principles for designing high-performance electrocatalysts. MOFs as a type of materials with well-defined structures are suitable to be studied as model catalysts for the fundamental study to unravel the true active sites for $CO_2RR$. Furthermore, given the nearly infinite number of potential metal nodes and coordinating organic linker combinations, MOFs display a wide range of chemical and structural variability, which makes them attractive catalyst candidates with tailorable properties for $CO_2RR$. However, low conductivity and stability remain the bottleneck of MOFs, which restricts their application in electrochemical $CO_2RR$[93]. In the past decades, it is demonstrated that the electrocatalytic performance can be improved by regulating the atomically dispersed metal catalytic sites and coordination environment around them in MOFs[163-166]. In this section, we focus on the molecular engineering of MOFs for enhanced $CO_2RR$ activity and selectivity toward desired products mainly based on the roles of metal nodes and coordinating organic ligands.

### 4.1 Regulation of metal nodes

MOFs with a periodic network structure possess uniformity and nearly 100% atomically dispersed sites, whose porous structure facilitates the adsorption and transport of $CO_2$[167]. The metal nodes of MOFs coordinated with organic ligands serve as active sites to speed up reaction rates, selectively transforming $CO_2$ to the desired products in a certain pathway. A family of typical two-dimensional (2D) flat MOFs [$TM_3(HAB)_2$, TM = Fe, Co, Ni and Cu; HAB = hexaaminobenzene] has been reported by Tang et al[168], in which TM bonded with four N atoms. According to

the calculations using DFT methods combined with the computational hydrogen electrode (CHE) model, $Fe_3(HAB)_2$ exhibited the strongest adsorption of *COOH and *H among these compounds, leading to the highest activity toward $CO_2$ production. The reaction pathway was proven to be a proton-assisted mechanism through a pathway of "$CO_2 \rightarrow$ *COOH $\rightarrow$ *CO $\rightarrow$ *CHO $\rightarrow$ *CHOH $\rightarrow$ *CH$_2$OH $\rightarrow$ CH$_3$OH". Thus, $Fe_3(HAB)_2$ was identified as a promising material catalyzing $CO_2$ to $CH_3OH$ via "RWGS (reverse water gas shift) + CO-hydro (CO hydrogenation)" process. Similarly, Cui et al.[169] also performed the calculation of conductive [$TM_3(HAB)_2$, TM = Fe, Co, Ni, Cu, and Mo]. Fe-, Co- and Ni-based MOFs presented weak adsorption of $CO_2$, while Cu-based MOFs exhibited strong adsorption energies of $CO_2$ and $H_2O$, with a higher interaction with $H_2O$ than with $CO_2$. In terms of Mo-based MOFs, they were identified as favorable candidates for adsorbing more $CO_2$ molecules than $H_2O$. The different charge density of $CO_2$ adsorbed on Mo-based MOFs displayed a distorted $CO_2$ molecule, indicating the good activation and selectivity of $CO_2$.

$M_3$(hexaiminotriphenylezne)$_2$, one type of conductive MOFs, known as $M_3(HITP)_2$ (M = Ni$^{2+}$, Cu$^{2+}$, HITP = hexaiminotriphenylezne), has been also applied to $CO_2RR$. The selectivity of $M_3(HITP)_2$ for $CO_2RR$ can be regulated by varying the metal nodes. A series of $M_3(HITP)_2$ (M = Fe, Co, Ni, Ru, Rh, and Pd) samples were investigated for $CO_2RR$ using DFT calculations. However, only $Co_3(HITP)_2$ and $Rh_3(HITP)_2$ exhibited superior selectivity toward $CH_3OH$ formation[170]. This was attributed to the strong chemical activity toward *COOH species and high *CO adsorption strength, which indicated the adsorbed $CO_2$ molecule can be activated and further reduced without desorption. $Co_3(HITP)_2$ and $Rh_3(HITP)_2$ with respective overpotentials of 0.67 V and 0.46 V exhibited superior catalytic activity. Similarly, the $CO_2RR$ performance of bis(iminothiolato)metals (marked as TMIT, TM = Mn, Fe, Co, Ni, Cu, Ru, Rh, and Pd, IT = $C_6S_3N_3H_3$) can be also affected by the metal nodes as simulated by spin-polarized calculations[171]. All these catalysts catalyzed $CO_2$ to produce HCOOH except that RuIT and RhIT only catalyzed CO production. This was because that the strong adsorption of CO on the RuIT and RhIT catalyst surfaces poisoned the catalysts. The π-conjugated metal bis(dithiolene) complex nanosheets ($M_3C_{12}S_{12}$, M = Fe, Co, Ni, Ru, Rh, and Pd)[172] within the spin-polarized frameworks were another typical type of MOFs. However, $Fe_3C_{12}S_{12}$, $Co_3C_{12}S_{12}$, $Ni_3C_{12}S_{12}$, and $Pd_3C_{12}S_{12}$ sheets exhibited weak chemical activity toward *COOH and *HCOO intermediates due to their high free energies ($\Delta G > 0.74$ eV), and thus these four catalysts were not considered to suit $CO_2RR$ applications. CO desorption and further hydrogenation on $Ru_3C_{12}S_{12}$ were indicated thermodynamically disadvantageous, while $Rh_3C_{12}S_{12}$ was suggested to be a potential catalyst for $CO_2RR$ due to its low free energy barrier and thus thermodynamical advantages. Additionally, a porous 2D graphene-like sheet $M_3(HHTQ)_2$ (M = Cu, Ni) was also constructed by a 2, 3, 7, 8, 12, 13-Hexahydroxytricycloquinazoline with Ni$^{2+}$ and Cu$^{2+}$ [140] (**Fig. 3a**). $Cu_3(HHTQ)_2$ showed stronger $CO_2$ adsorption than $Ni_3(HHTQ)_2$ and higher FE$_{CH3OH}$ up to 53.6 % at an overpotential of -0.4 V.

Doping diverse metal ions into MOFs is an attractive synthetic strategy to enhance the performance of $CO_2RR$ due to the unique characteristics introduced from the additional metal nodes, which may have synergistic effects[77, 78, 173-175]. For instance, Cho et al.[79] reported a series of zeolite-imidazolate frameworks (ZIF-8) containing Ni$^{2+}$, Fe$^{2+}$, and Cu$^{2+}$ (**Fig. 3b**). The $Cu_{0.5}Zn_{0.5}$/ZIF-8 achieved a higher FE of 88.5% for CO than the pristine ZIF-8 (43.7%), $Ni_{0.1}Zn_{0.9}$/ZIF-8 (34.7%) and $Fe_{0.3}Zn_{0.7}$/ZIF-8 (48.8%). This was because that the doped Cu affected the electronic structures of electron-rich sp$^2$ C sites via a local effect between the zinc-nitrogen (Zn-N$_4$) and copper-nitrogen (Cu-N$_4$) sites, which facilitated *COOH adsorption and promoted the reduction reaction. Iqbal et al.[54] reported bimetallic Ni and Fe in MOFs (MOF Ni-Fe). The incorporated combination of Ni and Fe metal centers increased the active surface area and active sites for the adsorption of intermediates, promoting the $CO_2RR$ process. As a result, the Ni and Fe bimetallic centers lowered the kinetic energy barrier, which achieved the FE$_{CO}$ of 98.2%, superior to single metal MOF-Ni (74.3%) and MOF-Fe (62.6%).

The construction of heteronuclear metal pair sites in MOFs can be used to regulate the kinetic energy barrier of intermediates formation for enhanced $CO_2RR$ performance. For instance, Zhong et al.[78] developed a layer-stacked 2D conjugated MOFs (PcCu-O$_8$-Zn) with CuN$_4$ (copper-phthalocyanine) and ZnO$_4$ (zinc-bis(dihydroxy)) to promote $CO_2$ into syngas (CO and H$_2$). The molar ratio of H$_2$/CO (1:7 to 4:1) was tuned by varying metal nodes (Cu and Zn) and applied potentials. The ZnO$_4$ showed high catalytic activity in converting $CO_2$ to CO, while the CuN$_4$ unit promoted the HER process. Synergistic catalytic effects were achieved by ZnO$_4$ and CuN$_4$ metal nodes. Another example was the integration of 2,3,9,10,16,17,23,24-octa-substituted metallophthalocyanine (MPc-XH, M = Co and Ni, X = N and O) into conductive MOFs as electrocatalysts for $CO_2RR$[77]. The activity and selectivity were tailored by the selection of metal nodes of MPcs and further adjustment of heteroatomic linkages. CoPc-Cu-O achieved an
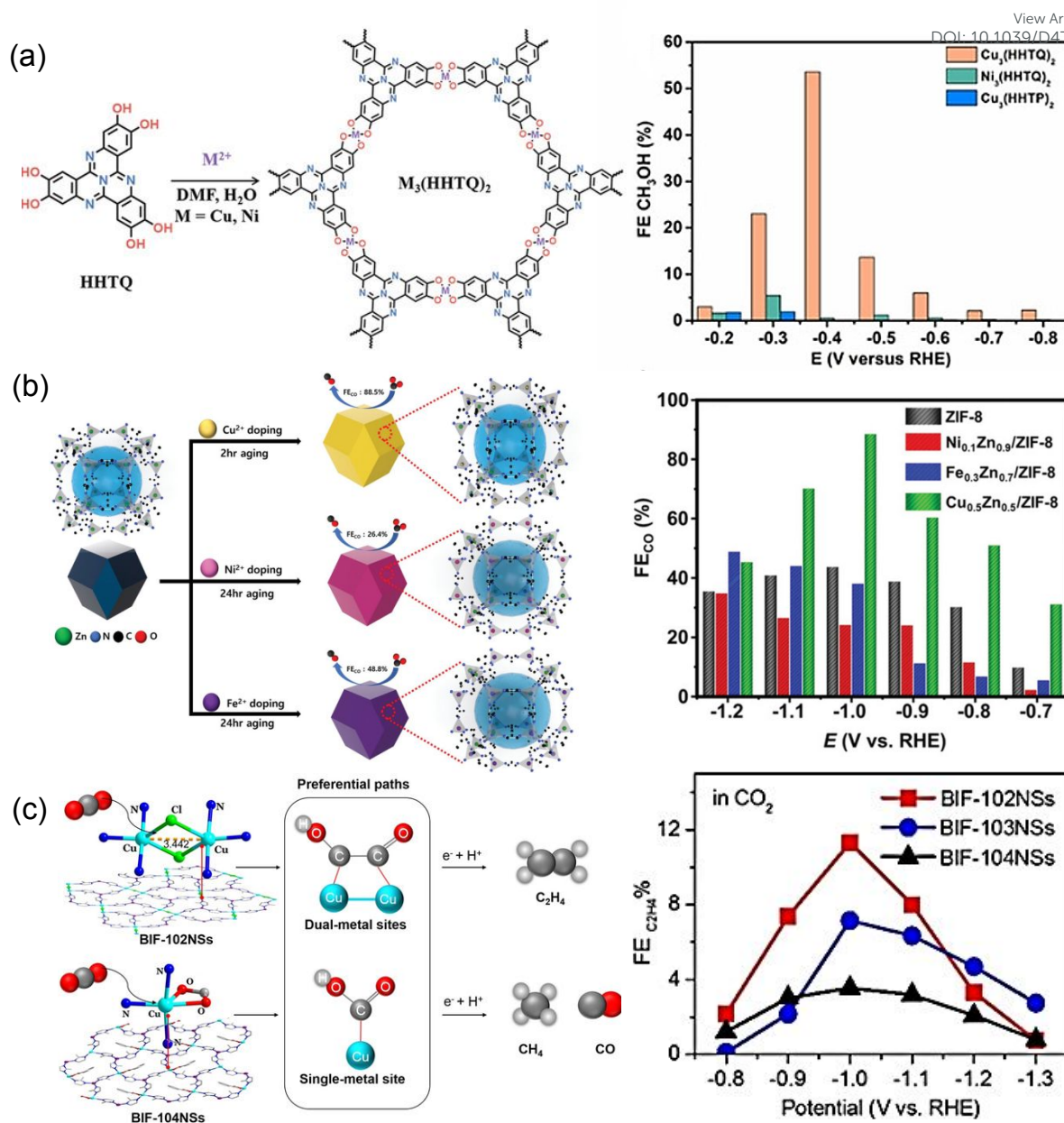
**Fig. 3** (a) Schematic synthesis of $M_3(HHTQ)_2$ (M = Cu, Ni) and FE of $CH_3OH$[140]. Copyright 2021, Wiley-VCH. (b) Schematic synthetic strategy of $M_xZn_y$/ZIF-8 catalyst and FE of CO[79]. Copyright 2023, Wiley-VCH. (c) Coordination environment and reaction pathways for BIF-102NSs and BIF-104NSs as well as FE of $C_2H_4$[127]. Copyright 2021, Wiley-VCH.

$FE_{CO}$ of 79% and a current density of -9.5 mA cm$^{-2}$. This is because that CoPc-based and O-linked MOFs lowered the activation energies toward *COOH formation, resulting in higher activity and selectivity. CuSn-HAB[145], a conductive 2D π-conjugated MOF with hexaiminobenzene (HAB) ligands and planar $Cu-N_4$ nodes, had a pair of $SnN_2O_2$ and $CuN_4$ sites bridged by $\mu$-N atoms and demonstrated an FE of 56% toward $CH_3CH_2OH$ formation. Further investigations revealed that the $SnN_2O_2$ site exhibited a higher affinity for O atoms compared with the copper site, playing an important role in promoting the formation of *$OCH_2$ intermediate. Therefore, the dual sites were more thermodynamically favorable for the C-C coupling between *CO and *$OCH_2$. In addition, Cu-Ni dual-metal sites

also showed similar synergistic effects for high selectivity[141]. The UiO-66(Hf) matrix helped for stabilizing the single atoms and facilitating ionizing radiation conversion, while atomic Cu-Ni dual-metal sites contributed to the high $CH_3OH$ selectivity. Under the radiation condition, CuNi SAs/UiO-66(Hf) realized selectivity of ~98% for $CH_3OH$ and energy efficiency of ~1.5 × 10$^{-7}$ mol J$^{-1}$. The spectral data and calculations showed that three $C_1$ intermediate adsorption states may occur at the Cu site and the final two at the Ni site, leading to selective $CH_3OH$ formation.

Similarly, the same nuclear metal pair also showed synergetic effects on the promoted performance of $CO_2RR$. (2,3,9,10,16,17,23,24-octahydroxyphthalo-cyaninato)

copper(II) (PcCu-(OH)$_8$) ligands and the CuO$_4$ nodes were used to construct a MOF catalyst (PcCu-Cu-O)[72]. PcCu-Cu-O with dual active sites exhibited high performance to convert CO$_2$ to C$_2$H$_4$ with a FE of 50% and a current density of 7.3 mA cm$^{-2}$. It was also found that dimer-copper catalysts Cu$^{II}_2$[BH(mim)$_3$]$_2$Cl$_2$ (BIF-102, BIF = Boron imidazolate frameworks, mim = 2-methylimidazole) with Cl$^-$ bridged dimer copper (Cu$_2$) units delivered high activity and selectivity for C$_2$H$_4$[127] (**Fig. 3c**). The enhanced performance was due to enriched charge around the dual Cu centers in Cu$^{II}_2$[BH(mim)$_3$]$_2$Cl$_2$ which performed as regulator for varying the energy barriers and afforded distinct reaction pathways. Therefore, Cu$^{II}_2$[BH(mim)$_3$]$_2$Cl$_2$ BIF-102NSs (NS = nanosheet) exhibited improved FE of C$_2$H$_4$ (11.3 %), superior to the iso-reticular BIF-103 (Cu$^{II}_2$[BH(mim)$_3$]$_2$(HCOO)$_2$, 7.15 %) and single-metal BIF-104 (Cu$^{II}$[BH(mim)$_3$](BA), 3.55 %).

MOFs containing multi-metallic redox-active secondary building units (SBUs) have also been reported to be good candidates for high-performing electrocatalysts. Huang et al. reported an alkali-resisting MOF (Cu$_1$Ni-1,4-benzenedipyrazolate, Cu$_1$Ni-BDP) featuring pyrazolate-stabilized asymmetric Ni/Cu clusters sites for CO$_2$RR[176]. The unique Ni-Cu hybrid sites, characterized by an asymmetric electronic structure, orbital interaction and close distance (2.8 Å), synergistically catalyzed the conversion of CO$_2$ to C$_2$H$_4$. In the alkaline environment (1.0 M KOH), The Cu$_1$Ni-BDP exhibited a notable C$_2$H$_4$ selectivity, yielding an FE of 52.7% and a partial current density of 278 mA·cm$^{-2}$ at -1.3 V. Moreover, only a 4.5% decrease in FE observed after 25 h electrolysis. Operando analyses and theoretical calculations indicated that the asymmetric Ni/Cu sites effectively reduced the energy barrier associated with *COH-COH intermediate, the rate-limiting step in CO$_2$ reduction to C$_2$H$_4$. MOFs containing hetero bimetallic clusters sites offer the potential for synergistic catalysis or tandem catalysis toward C$_{2+}$ production. Similarly, a two-dimensional Ru$_2$(OAc)$_4$Ni(CN)$_4$, featuring Ru and Ni bimetallic metal sites was reported to exhibit high activity and selectivity for 1-C$_4$H$_8$ production[177]. At room temperature, it achieved a production rate of 1.3 mol g$_{cat}^{-1}$·h$^{-1}$ and conversion efficiency of 97%. Trinuclear clusters within MOFs have also been proven to be effective in electrochemical CO$_2$RR to produce value-added products. Huang et al[130] reported a low-cost metal-azolate framework [Cu$_3$(μ$_3$-OH)(μ$_3$-trz)$_3$(OH)$_2$(H$_2$O)$_4$](Cutrz) constructed by 1H,1,2,4-triazole (Htrz) organic ligands and Cu$_2$SO$_4$·5H$_2$O salts. The Cutrz MOF with trinuclear clusters as the active sites displayed a high FE of 50% to selective electroreduction of CO$_2$ to C$_2$H$_4$. The trinuclear cluster {Cu$_3$(μ$_3$-OH)(μ$_3$-trz)$_3$}$^{2+}$ enabled the simultaneous adsorption of three *CO intermediates on its surface, positioning closely at only 3.3 Å apart. This close proximity led to a higher *CO coverage and facilitated C-C dimerization coupling with a reduced energy barrier. By tailoring the size of the monodispersed CuTrz, the catalyst's performance was further enhanced to 55.4%[132]. CuTrz particles with an average size of 109 nm showed superior activity compared to the larger counterparts. Extensive characterizations revealed that the remarkable selectivity was attributed to the uniform small size of the CuTrz and the presence of abundant grain boundaries.

## 4.2 Modulation of surrounding organic ligands

Though metal nodes of MOFs play a significant role in determining the activity and selectivity of CO$_2$RR, it is important to note that the same type of metal nodes in different MOFs may result in different pathways toward different carbon products. The variation in catalytic behaviors may be attributed to differences in the electronic properties of the metal nodes in different types of MOFs, including their oxidation state[178, 179] and electron density[180], which are significantly influenced by the metal coordination geometry and ligand environment. In this section, the important contribution from the ligands surrounding the metal nodes of MOFs to CO$_2$RR is discussed. In general, organic ligands in MOFs play an essential role in regulating the specific sizes, geometries, and symmetries[181]. It is considered that MOFs can achieve outstanding catalytic activity and stability to CO$_2$RR through rational design of building blocks with specific functional groups, side structures and modified with small molecules[88, 182]. The regulation strategy generally includes the modulation of the side groups and the body structure of organic ligands.

By changing the size of ligand side groups, Cu(I) triazolate frameworks (MAF-2ME, MAF-2E, and MAF-2P) were tailored to realize high-efficiency conversion of CO$_2$ to C$_2$H$_4$/CH$_4$[53] (**Fig. 4a**). The C$_2$H$_4$/CH$_4$ selectivity ratio can be tuned and inversed from 11.8: 1 to 1: 2.6 with selectivity up to 51 % (C$_2$H$_4$), 56 % (CH$_4$), and 77 % (hydrocarbon), respectively. Computational simulations showed that the geometry structure of Cu(I) changed from triangular to tetrahedral due to the change of ligand side groups, with two adjacent Cu(I) cooperating for C-C coupling to form C$_2$H$_4$. Recently, Mao et al.[183] synthesized Cu-based MOFs with an optimal Cu-Cu distance, named MIL-53 (Cu) (MIL = Materials of Institute Lavoisier) (**Fig. 4b**). Ten different ligand side groups from electron-donating groups (NH$_2$, CH$_3$, NHOH, OH, and H) to electron-withdrawing groups (COOH, Cl, Br, CN, and NO$_2$) were chosen to decorate the organic ligand in MIL-53 (Cu) to modulate the Cu-Cu distance and charge of Cu. COOH-ligand-decorated MIL-53 (Cu) was located at the top of the volcano plot and exhibited the highest catalytic activity and selectivity toward CH$_3$CH$_2$OH production. COOH-ligand-decorated MIL-53 (Cu) exhibited its high catalytic performance with an FE of 55.5%, which was superior to the Cu electrode (35.7% at -1.05 V *vs*. RHE). Similarly, Nam et al.[87] added side groups of -NH$_2$ in a face-centered cubic (*fcu*) MOF to strengthen the adsorption capacity of CO$_2$ (**Fig. 4c**). As a result, FE$_{CO}$ increased and FE$_{H2}$ decreased on Ag/Zr-*fcu*-MOF-NDC (H$_2$BDC: 1,4-benzenedicarboxylic acid) than on Ag/Zr-*fcu*-MOF-BDC and Ag/Zr-*fcu*-MOF-NH$_2$BDC. They also explored the role of body structure of ligands in modifying the binding modes of *CO intermediates, which played a pivotal role in product selectivity. The high CO$_{bridge}$ population in Ag/Zr-*fcu*-MOF-NDC (H$_2$NDC: 1,4-naphthalenedicarboxylic acid) made for enhanced CO selectivity. Aromatic amine groups was also coupled into a silver chalcogenolate cluster-based MOF (Ag$_{12}$(S$^t$Bu)$_8$(CF$_3$COO)$_4$(bpy-NH$_2$)$_4$, denoted as 1-NH$_2$, aka-Ag$_{12}$bpy-NH$_2$, bpy-NH$_2$ = 3-amino-4,4'-bipyridine) to capture CO$_2$ molecules in a simulated flue gas and served as CO$_2$ catalytic sites[91] (**Fig. 4d**). The 1-NH$_2$ MOF
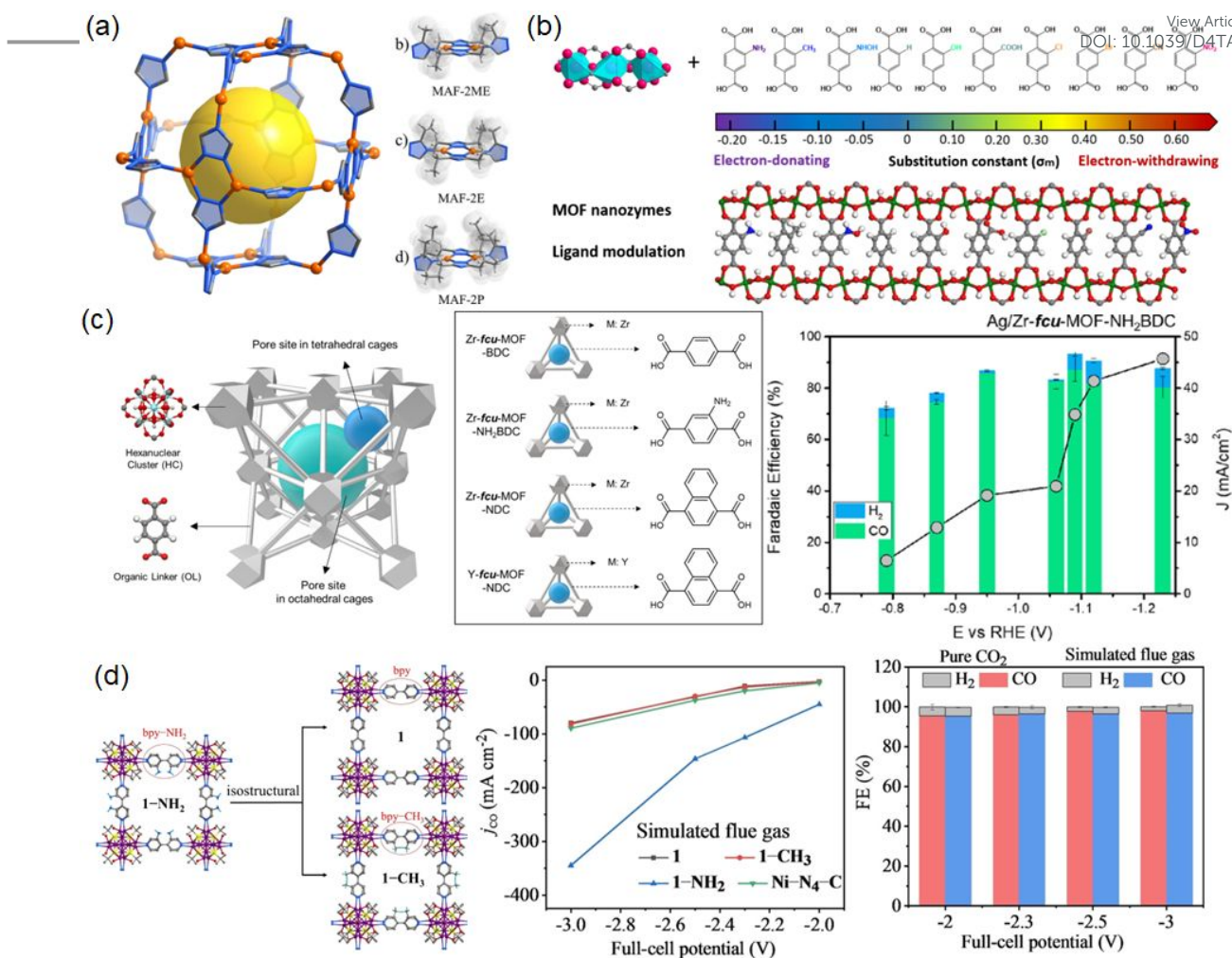
**Fig. 4** (a) Crystal structures and local coordination environments of MAF-2 analogs[53]. Copyright 2022, Wiley-VCH. (b) Ten possible ligand-decorated 1,4-benzenedicarboxylic acid linkers with their substituent constant values[183]. Copyright 2023, American Chemical Society. (c) MOF design strategies based on the Zr-***fcu***-MOF-BDC MOF and FE of CO for Ag/Zr-***fcu***-MOF-NH$_2$BDC[87]. Copyright 2020, American Chemical Society. (d) Schematic of 1, 1-CH$_3$ and 1-NH$_2$, $j_{CO}$ of 1, 1-CH$_3$, 1-NH$_2$ and Ni-N$_4$-C catalysts under simulated flue gas and FE$_{CO}$ for 1-NH$_2$ in CO$_2$ and simulated flue gas[91]. Copyright 2023, Wiley-VCH.

could catalyze the adsorbed CO$_2$ into CO with an ultra-high CO$_2$ conversion of 60 % and a FF$_{CO}$ of 96 % due to the introduction of the aromatic amine groups, better than [Ag$_{12}$(S$^t$Bu)$_8$(CF$_3$COO)$_4$(bpy)$_4$] (bpy: 4,4'-bipyridine, 1, aka Ag$_{12}$bpy) and [Ag$_{12}$(S$^t$Bu)$_8$(CF$_3$COO)$_4$(bpy-CH$_3$)$_4$] (bpy-CH$_3$: 3-methyl-4,4-bipyridine, 1-CH$_3$, aka Ag$_{12}$bpy-CH$_3$).

Modifying the body structure of organic ligands has also been reported as an effective strategy to enhance CO$_2$RR performance. For instance, changing the ligand body structure of ligand linkers in Cu naphthalenedicarboxylate (Cu-UNDC) and Cu benzenedicarboxylate (Cu-UBDC) can regulate the MOFs structure and electronic environment of Cu centers, thus changing the selectivity toward C$_2$ products[184] (**Fig. 5a**). The two catalysts showed different FEs for C$_2$ products. FEs for Cu-UBDC were (13.2% in the dark and 26.2% in the light. FEs for Cu-UNDC were 24.3% in the dark and 21.8% in the light. Moreover, in-built heteroatoms within the molecular structure of organic ligands leads to significant variations in electrocatalytic CO$_2$RR. Liu et al.[124] designed and synthesized a 2D conjugated Cu MOF

(HATNA-Cu-MOF) by coordination of an electron-deficient N-containing conjugated molecule HATNA-6OH (hexaazatrinaphthylene) and Cu(NO$_3$)$_2$. The symmetric aromatic heterocycle of HATNA-6OH with 6 hydroxyl groups makes it selectively coordinate with Cu$^{2+}$ in a 2D framework, with three phenanthroline units as additional sites for guest binding. The synergistic effects of HATNA and copper catecholate node enabled the conjugated HATNA-Cu-MOF to selectively convert CO$_2$ to CH$_4$ with an FE of 78 % at -1.5 V. The tailoring of ligands can adjust both coordination microenvironment of metal nodes and geometry structure of MOFs, thereby affecting their electronic structure and interaction with intermediates. Recently, a series of Cu(I)-based MOFs ([Cu$_4$X(TIPE)$_3$]·3X, [X = Cl, Br, I, TIPE = 1,1,2,2-tetrakis(4-(imidazol-1-yl)phenyl)ethene] with different coordination microenvironments (Cu-Cl, Cu-Br,
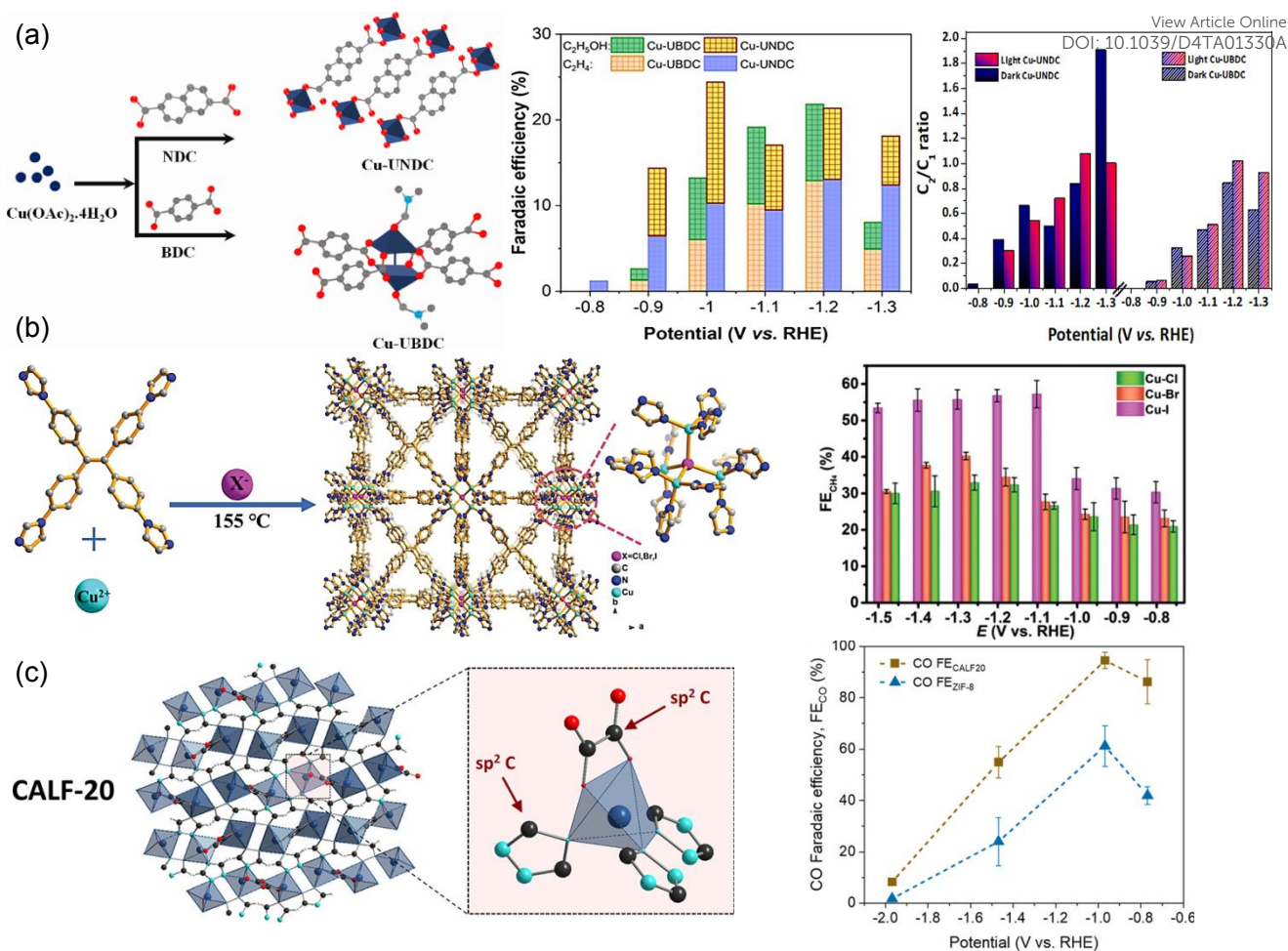
**Fig. 5** (a) Schematic, FE toward $C_2$ products and $C_2/C_1$ ratio of Cu-UNDC and Cu-UBDC in $CO_2$-saturated 0.1 M $KHCO_3$[184]. Copyright 2023, American Chemical Society. (b) Schematic illustration of the structure and $FE_{CH_4}$ of Cu-X (X = Cl, Br and I)[52]. Copyright 2022, Wiley-VCH. (c) Schematic illustration of the crystal structure of CALF20 and $FE_{CO}$ of ZIF-8 and CALF20[88]. Copyright 2021, American Chemical Society

and Cu-I) were synthesized by Sun et al.[52] (**Fig. 5b**). With increasing radius of halogen atoms from Cl to I, the $CO_2$ adsorption increased and d-band center of Cu positively shifted to the Fermi level, resulting in enhanced selectivity of $CO_2$ to $CH_4$. The shifted d-band center reduced the formation energies of $*CH_2O$ and $*CH_3O$ species from Cl to I and thus enhanced the electrocatalytic activity. The MOF with $Cu_4I$ cluster (X = Cl, Br and I) gave partial current density of 60.7 mA $cm^{-2}$ and FE of 57.2% for $CH_4$ production at -1.08 V compared with Cu-Cl (32.9%) and Cu-Br (40.2%) at -1.28 V. Al-Attas et al.[88] explored Zn-based MOFs with two different azolate functional ligands, 1,2,4-triazole (Calgary Framework 20, CALF20, [$Zn_2(Tz)_2Ox$]) and 2-methylimidazole (zeolitic imidazolate framework-8, ZIF-8, [$Zn(MeIm)_2$]) for $CO_2RR$ (**Fig. 5c**). CALF20 showed higher FE for CO (94.5%) compared to ZIF-8 (61.1%). The $sp^2$ carbon atoms in 1,2,4-triazole ligands coordinated with the Zn(II) centers were claimed as the active sites for $CO_2RR$, as 3d orbital of Zn(II) centers were fully occupied. In addition, ab initio investigation showed that the N-$sp^2$ C adsorption site was the most favorable adsorption sites in CALF20 and ZIF-8. 1,2,4-triazole ligand in

CALF20 with more electrons induced in the adjacent active sites enhanced the charge transfer and facilitated $*COOH$ formation, promoting CO production with high current density and FE. The researchers further assembled the CALF20 into a gas diffusion electrode and realized a 95% FE for converting $N_2$-diluted $CO_2$ streams to CO[185].

## 4.3 Post-modification

As a matter of fact, incorporation of functional modules into MOFs for enhancing $CO_2RR$ performance can be realized not only through direct synthesis but also through post-modification. Therefore, doping extraneous ligands in MOFs is one of the most effective strategies. For example, ZIF， a subclass of MOFs assembled by metal nodes and imidazole ligands, exhibited excellent thermal and chemical stability with various topologies[76]. The active sites were considered to be the imidazolate ligands coordinated with the Zn(II) nodes in ZIFs with ZIF-8 showing the highest $FE_{CO}$ of 81.0% and a current density of 12.8 mA $cm^{-2}$ [76]. Later, Dou et al.[81] developed a ligand doping strategy by introducing 1,10-phenanthroline into ZIF-8

using post-treatment process. The conjugated structure of 1,10-phenanthroline might benefit from electron delocalization and increased the electron density around nitrogen, thereby facilitating π electron transfer and enhancing σ electron
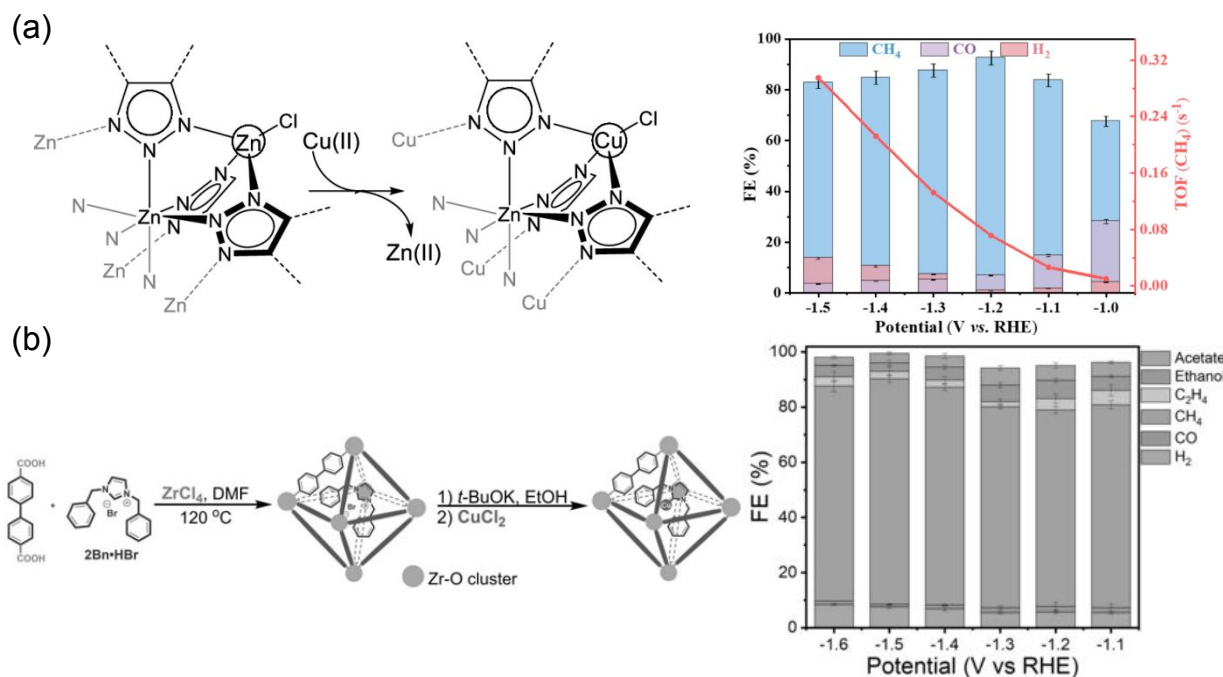


**Fig. 6** (a) Schematic of metal transformation process, $FE_{CH4}$ and TOF of $Cu_4^{II}$-MFU-4*l*[69]. Copyright 2021, American Chemical Society. (b) Schematic synthesis route and FE of 2Bn-Cu@UiO-67[126]. Copyright 2021, Wiley-VCH.

donation between nitrogen and metal[186]. In this study, 1,10-phenanthroline acted as electron donor induced the adjacent $sp^2$ C atoms in imidazolate and thus strengthened the ability of *COOH formation, delivering a high FE of 90.57%. Also, metallocene[93] had a similar impact on the improvement of electron conductivity and electron-donating ability. Using chemical vapor deposition method, metallocene was implanted in MOF-545-Co. The as-prepared $CoCp_2$@MOF-545-Co selectively converted $CO_2$ to CO with an FE of 97% due to its strong binding interaction, which reduced the adsorption energy of $CO_2$. This method can be applied universally to other materials. For instance, diphenyl sulfide immobilized onto graphene served as an axial ligand for tetraphenylporphyrin cobalt (PCo), while [PCo]*- acted as active sites promoting $CO_2$ reduction[187]. The benzene rings of diphenyl sulfide stacked with graphene with a face-to-face manner, serving as a mediator to the electron transfer communication between PCo and graphene.

Doping extra metal elements in MOFs was an effective method to prepare high-efficiency MOF electrocatalysts. Recently, a new 2D BIF-73-NS (BIF = boron imidazolate framework, $CdBH(im)_3 \cdot (dobdc)_{0.5} \cdot DMF$, im = imidazolate, $H_2dobdc$ = 2,5-dihydroxyterephthalic acid, DMF = dimethylformamide) nanosheet was successfully synthesized through ultrasonication exfoliation of bulk BIF[80]. Benefiting from the functional -OH groups, Fe ions were anchored, and molecular-level $Fe_2O_3$ were formed in 2D BIF-73-NS. The 2D BIF-73-NS with $Fe_2O_3$ fragments exhibited a high $FE_{CO}$ of 88.6% at -

1.8 V *vs* Ag/AgCl. In addition, Zhu et. al.[69] prepared $Cu_4^{II}$-MFU-4*l* by exchanging partial Zn(II) ions in MFU-4*l* ([$Zn_5Cl_4(btdd)_3$], $H_2btdd$ = bis(1H-1,2,3-triazolo-[4,5-b], [4',5' -i]dibenzo-[1,4]-dioxin)) with Cu(II) irons (**Fig. 6a**). *In situ* X-ray absorption spectroscopy (XAS) and infrared (IR) spectroscopy spectra revealed that the $Cu(I)N_3$ were *in situ* formed from Cu(II) species, acting as active sites. $Cu(I)N_3$ showed strong coordination ability and synergistic effects with adjacent aromatic hydrogen atoms, playing an important role in stabilizing the key intermediates and suppressing the competitive HER, thus showing high electrocatalytic activity and selectivity for $CH_4$ formation (FE = 92%).

Additionally, encapsulation strategy was also proposed to prepare MOF electrocatalysts with enhanced performance in $CO_2RR$. Chen et al.[126] encapsulated N-heterocyclic carbene molecules (NHCs, 1,3-dibenzyl-1H-imidazol-3-ium bromide, 2Bn · HBr) into the UiO-67 for their well-matched molecular size. Cu was added to the alkaline medium to synthesize 2Bn-Cu@UiO-67 (**Fig. 6b**). Due to the acidic C-H bond of the imidazole, NHCs with a lone pair of electrons tended to bond with the metal to generate a stable NHC-metal complex. The 2Bn-Cu@UiO-67 achieved 81 % FE of $CH_4$ and a high TOF of 16.3 $s^{-1}$. It was suggested that σ donation of NHC enhanced the surface electron density of Cu catalytic sites and optimized the adsorption of *CHO species.

A novel 3D framework **1'** {[$Ni_3Zr_6(\mu_3$-O)$_4(\mu_3$-OH)$_4(IN)_{12})(H_2O)_6$] · $Cl_6$ · 4DMF · $18H_2O$}$_n$ with [$Zr_{48}Ni_6$] nano-cages was constructed to confine Au nanoparticles (**Fig. 7a**)[55].

The porous framework **1'** exhibited high surface area and good stability which allowed selectively extract $AuCl_4^-$ ions from electronic waste. The $AuCl_4^-$ was further reduced into Au nanoparticles and thus formed Au nanoparticles@**1'** hybrid materials (Au NPs@**1'**-*x, x* = 1, 2, 3, and 4) with different Au nanoparticle sizes. By controlling loading amounts, the sizes of
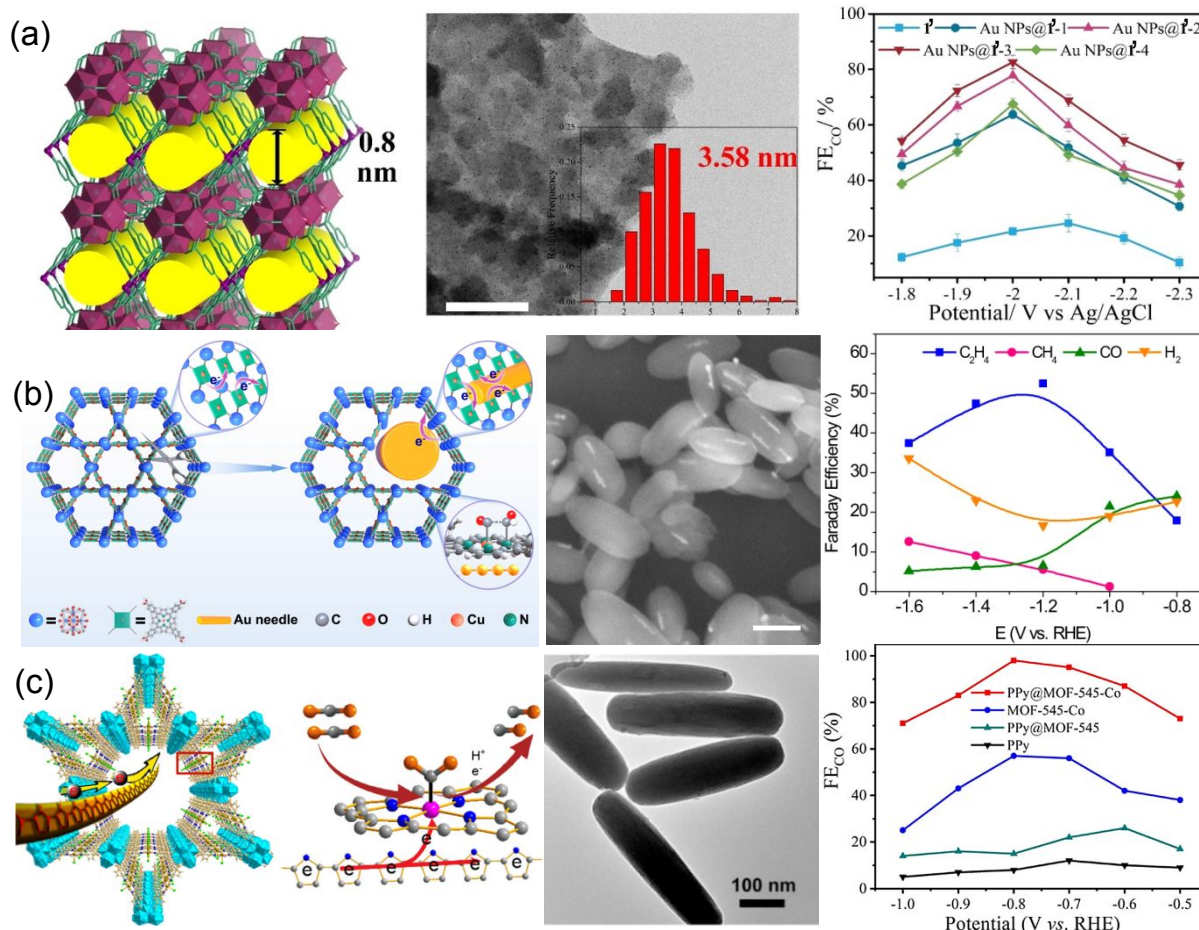


**Fig. 7** (a) Three-dimensional framework of **1'**, TEM image of Au-NPs@**1'**-3 and $FE_{CO}$ of Au NPs@**1'**-*x* (*x* = 1, 2, 3, and 4)[55]. Copyright 2022, Wiley-VCH. (b) Schematic illustration, SEM image and FE for different products of the AuNN@PCN-222(Cu) catalyst[188]. Copyright 2022, Springer Nature. (c) Schematic illustration for the advantages of PPy in the MOF-545-Co, TEM image of PPy@MOF-545-Co and $FE_{CO}$ of PPy@MOF-545-Co under different voltages[189]. Copyright 2021, American Chemical Society

Au NPs were tunable. Au NPs@**1'**-3 exhibited a $FE_{CO}$ of 95.2 % with a current density of 102.9 mA $cm^{-2}$ at -1.1 V and remained stable for more than 15 h. The excellent stability was attributed to the confinement effect of **1',** which avoided the agglomeration of Au NPs. Inspired by the CO generator of Au and coupling of $Cu-N_4$ active sites, Au nanoneedles were impregnated into PCN-222 MOF (PCN = porous coordination networks) to construct AuNN@PCN-222(Cu) with the assistance of reducibility of carboxylate ligands (**Fig. 7b**)[188]. AuNN@PCN-222(Cu) with metalloporphyrin Cu centers achieved an FE of 52.5% for $C_2H_4$ and exhibited better structural stability. Through *operando* X-ray spectroscopy, *in situ* infrared spectroscopy and DFT calculations, the enhanced selectivity was ascribed to the C-C coupling in a tandem catalysis mechanism. The CO generated at the Au nanoneedles and then was abducted to *CHO at the Au-activated N motifs. The catalyst thus exhibited

excellent $C_2H_4$ selectivity and high FE. Furthermore, the Au-inserted catalyst also showed improved structural stability, due to the altered charge conduction pathway bypassing the reticular network. A similar case of an electron-conductive polypyrrole (PPy) molecule was also reported, which was inserted into the channel of MOFs through the *in situ* low-temperature polymerization of pyrrole in the pore of PPy@MOF-545-M (M = Fe, Co, and Ni) (**Fig. 7c**)[189]. The MOF-545-Co with increased electron-transfer ability presented excellent electrocatalytic $CO_2RR$ performance. The $FE_{CO}$ of PPy@MOF-545-Co reached 98% at -0.8 V, which was approximately two times higher than that of bare MOF-545-Co. Such high performance was attributed to the incorporation of PPy that serves as electric cables in the channel of MOFs, facilitating electron transfer during the $CO_2RR$ process.

**ARTICLE**

# 5. MOF derivatives

MOFs usually face many challenges, such as limited active sites, unsatisfying electrical conductivity, and stability issues. This results in the generation and development of MOF derivatives with robust structure and good conductivity as electrocatalysts for CO$_2$RR.

## 5.1 MOF derivatives through wet chemistry method

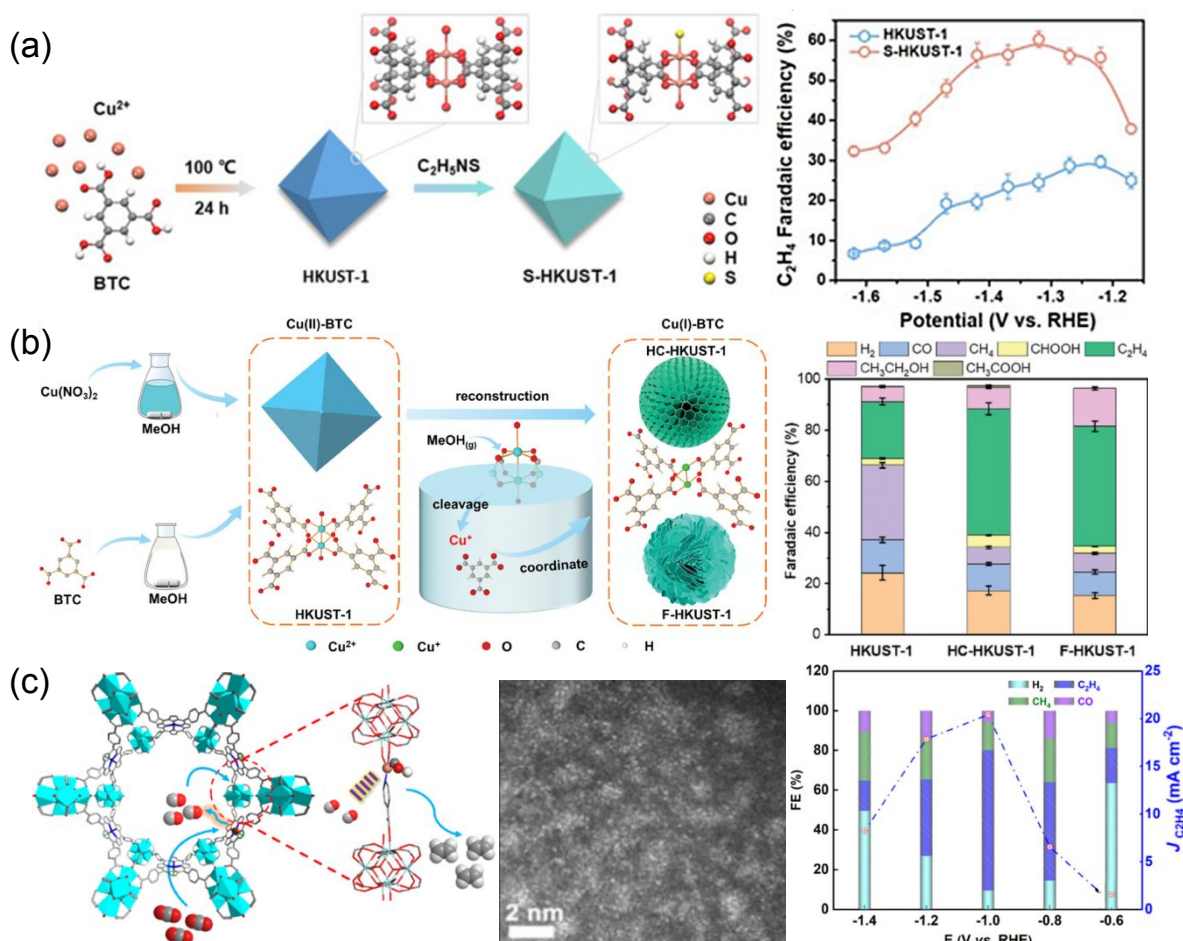Structural transformation strategy by wet chemistry method to obtain MOF derivatives at mild temperature is



**Fig. 8** (a) Schematic illustration depicting the preparation of S-HKUST-1 and FE of C$_2$H$_4$ at different potentials[134]. Copyright 2021, Wiley-VCH. (b) Schematic illustration of the synthetic procedures for the HC-HKUST-1 and F-HKUST-1[190]. Copyright 2024, Wiley-VCH. (c) Schematic illustration of the Cu-SAs@Ir-PCN-222-PA tandem electrocatalyst[57]. Copyright 2024, American Chemical Society.

fascinating as it maximizes the preservation of the original coordination structure and geometric morphology. As an example, S-HKUST-1 was prepared by immersing HKUST-1 in an ethanol solution containing thioacetamide (**Fig. 8a**)[134]. Thioacetamide reacted with the water in HKUST-1 to produce H$_2$S, facilitating the formation of Cu-S bonds. The element distribution, XRD and Fourier transform infrared spectra indicated that the sulfur is distributed throughout the S-HKUST-1 particle, with the framework structure and organic bonding of HKUST-1 well maintained. Operando X-ray absorption and systematic characterizations confirmed that the stable Cu-S

motif of S-HKUST-1 during CO$_2$ reduction reaction. The atomically dispersed Cu-S units in S-HKUST-1 exhibited high selectivity to C$_2$H$_4$ with a maximum FE of 60.0% in an H-type cell and up to 57.2 % in a flow cell. The partially oxidized Cu$^{\delta+}$ at the Cu/Cu$_x$S$_y$ interfaces and the optimized geometric and electronic structures for *CO dimerization, played a crucial role in reducing the kinetic barriers for the CO$_2$ reduction process. Utilizing a "reduction-cleavage-recrystallization" method (**Fig. 8b**)[190], the Cu(II)-BTC (HKUST-1) underwent a conversion to Cu(I)-BTC facilitated by methanol vapor, followed by reconstruction in a methanol solution. The liquid/solid-gas interface played an

**Journal Name**

**ARTICLE**

important role in the transformation to Cu(I)-BTC, altering the oxidation state of Cu and the coordination environment of the metal node. The Cu(I)-BTC showed improved $C_2H_4$ selectivity with an FE up to 57% at -1.6 V and exceptional durability over for 38 h, superior to both the flower-like HKUST-1 (F-HKUST-1) and HKUST-1 catalysts. The superior performance was attributed to the Cu(I)-O coordinated structure and the presence of free carboxyl groups, which enhanced the dimerization of *CO intermediates and hindered the hydrogenation of *CO intermediate. In another report, Cu single atoms were incorporated into the Ir-PCN-222 MOF to create Cu-SAs@Ir-PCN-222-PA by stirring a mixture of metal precursor Cu-PA (PA = 4-picolinic acid) and Ir-PCN-222-PA at 140 °C for 12 h (**Fig. 8c**)[57]. The dual active sites of Ir-porphyrin and Cu-SAs enabled tandem catalysis for conversion of $CO_2$ to $C_2H_4$. CO was initially produced on Ir-porphyrin and then transferred to the nearby adsorbed *CO intermediate on Cu-SAs to facilitate the C-C coupling process. The tandem catalysis led to the production of $C_2H_4$ from $CO_2$ with an FE of 70.9% in a flow cell and 66.9% in an H-cell.

### 5.2 MOF-derivatives through pyrolysis treatment
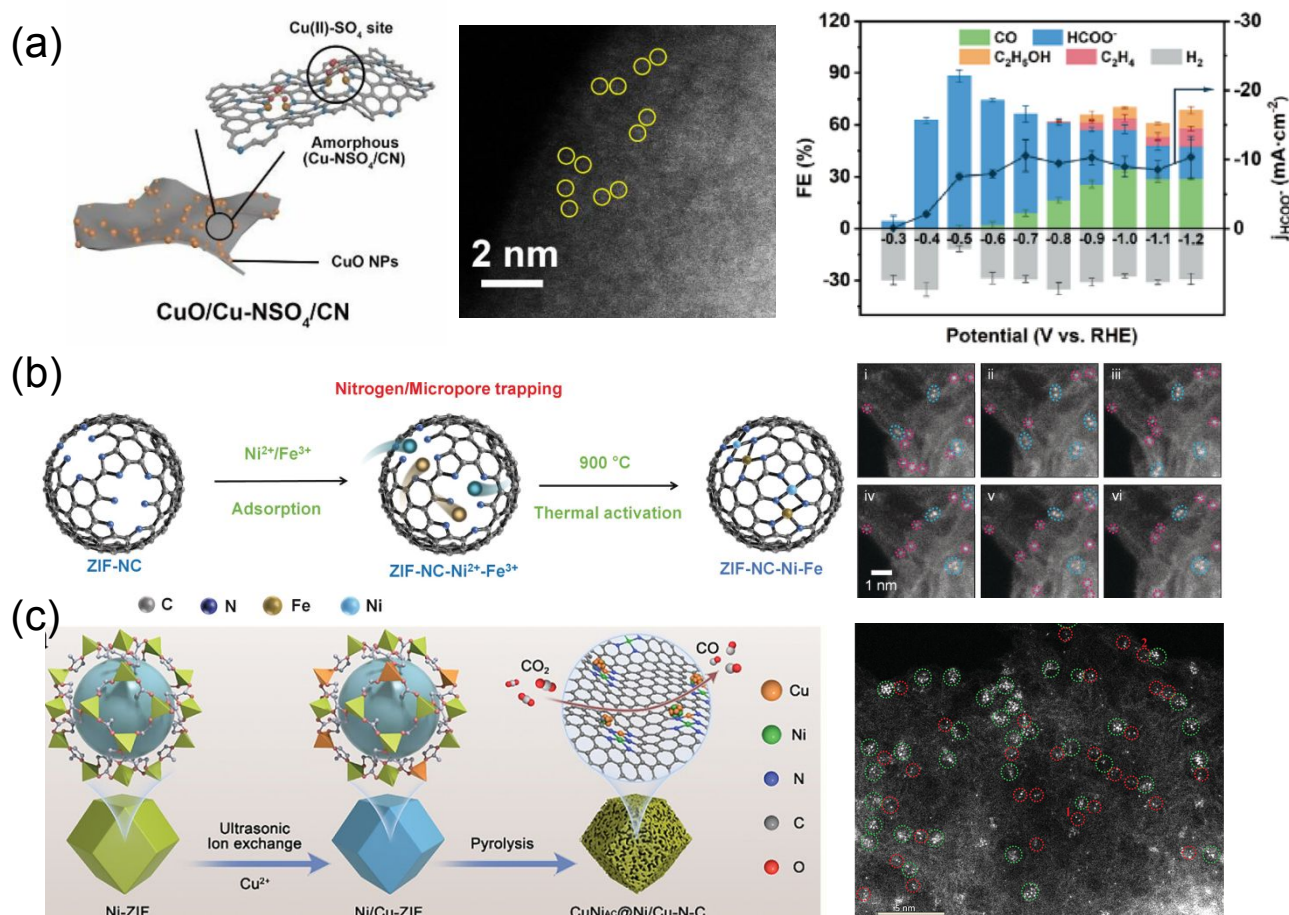


**Fig. 9** (a) Schematic illustration of the structure, aberration-corrected HAADF-STEM and FE of CuO/Cu-NSO$_4$/CN[193]. Copyright 2024, Wiley-VCH. (b) Schematic illustration and HAADF-STEM of dual metal Ni-Fe sites in ZIF-NC-Ni-Fe [95]. Copyright 2022, Wiley-VCH. (c) Schematic diagram depicting the preparation of CuNi$_{AC}$@Ni/Cu-N-C [194]. Copyright 2024, Wiley-VCH.

## ARTICLE

The process of structural transformation occurring at elevated temperatures is commonly referred to pyrolysis or annealing. This process involves not only the reduction of ions to atoms but also the conversion of organic frameworks into carbon skeletons. High-temperature pyrolysis plays a crucial role in the creation of single-atom catalysts (SAC) and the introduction of heteroatoms through doping. This strategy allows for the regulation of the coordination environment of MOF-derived carbonaceous SACs for enhancement of $CO_2RR$ performance.

### 5.2.1 Metal centers

The metal centers in MOF-derived M-N-C catalysts, akin to pristine MOFs usually determine the performance of $CO_2RR$. A highly ordered hierarchical porous catalyst, HP-FeNC with $Fe-N_4$ moieties was prepared through the template method[191], leading to an a maximum $FE_{CO}$ of 96% at -0.5 V and partial current density of -19 $mA·cm^{-2}$. Compared with Fe-N-C catalysts, Ni-N-C catalysts were seldom reported for $CO_2$ reduction due to the susceptible breakage of Ni-N bonds at high temperature[192]. However, the deprotonated form of Ni-N-C is dominant in neutral or weakly acidic electrolyte, suppressing HER activity with high-efficiency $CO_2RR$. With the assistance of $ZnCl_2$ and KCl[45], a microwave-assisted rapid pyrolysis method was employed to derive the Ni-N-C electrocatalyst from a Ni-doped ZIF-8 in just 3 min under air atmosphere. The obtained $Ni_1$-N-C-50 with a mass ratio of KCl/Ni-ZIF-8 at 50, showcased a $Ni-N_4$-C configuration and presented a remarkable $FE_{CO}$ of 96% in a flow cell, surpassing the traditional pyrolysis of $Ni_1$-N-C in a furnace. Mechanistic investigations revealed that the microwave-assisted method assisted by $ZnCl_2$/KCl resulted in abundant defective sites and mesoporous structure, which facilitated $CO_2$ activation and accelerated mass transfer. Furthermore, Cu was explored as an intriguing element. In contrast to Fe and Ni, Yuan et al.[193] reported a $CuO/Cu-NSO_4/CN$ catalyst produced by incomplete pyrolysis of sulfate-modified CuOS-NBDC MOF at 400°C in air **(Fig. 9a)**. The anionic groups not only stabilized the metal sites but also modified the electronic structure, which reduced $CO_2$ to formates with a high FE of 87.4% at -0.5 V. The sulfate played a crucial role in promoting the conversion of $CO_2$ to carboxyl intermediates, subsequently being hydrogenated to HCOOH. The universal modification strategy can be also applied to the preparation of Fe-, Co and Ni- and Zn(II)-based catalysts for catalytic reaction.

In addition to the active sites, recognized as independent units, the adjacent metal sites can largely affect the performance of $CO_2$ reduction reaction. Jiao et al.[46] prepared Fe and Ni single-atom pairs on MOF-derived N-doped carbons ($Fe_1$-$Ni_1$-N-C) by the direct pyrolysis of MOFs. Due to the synergistic

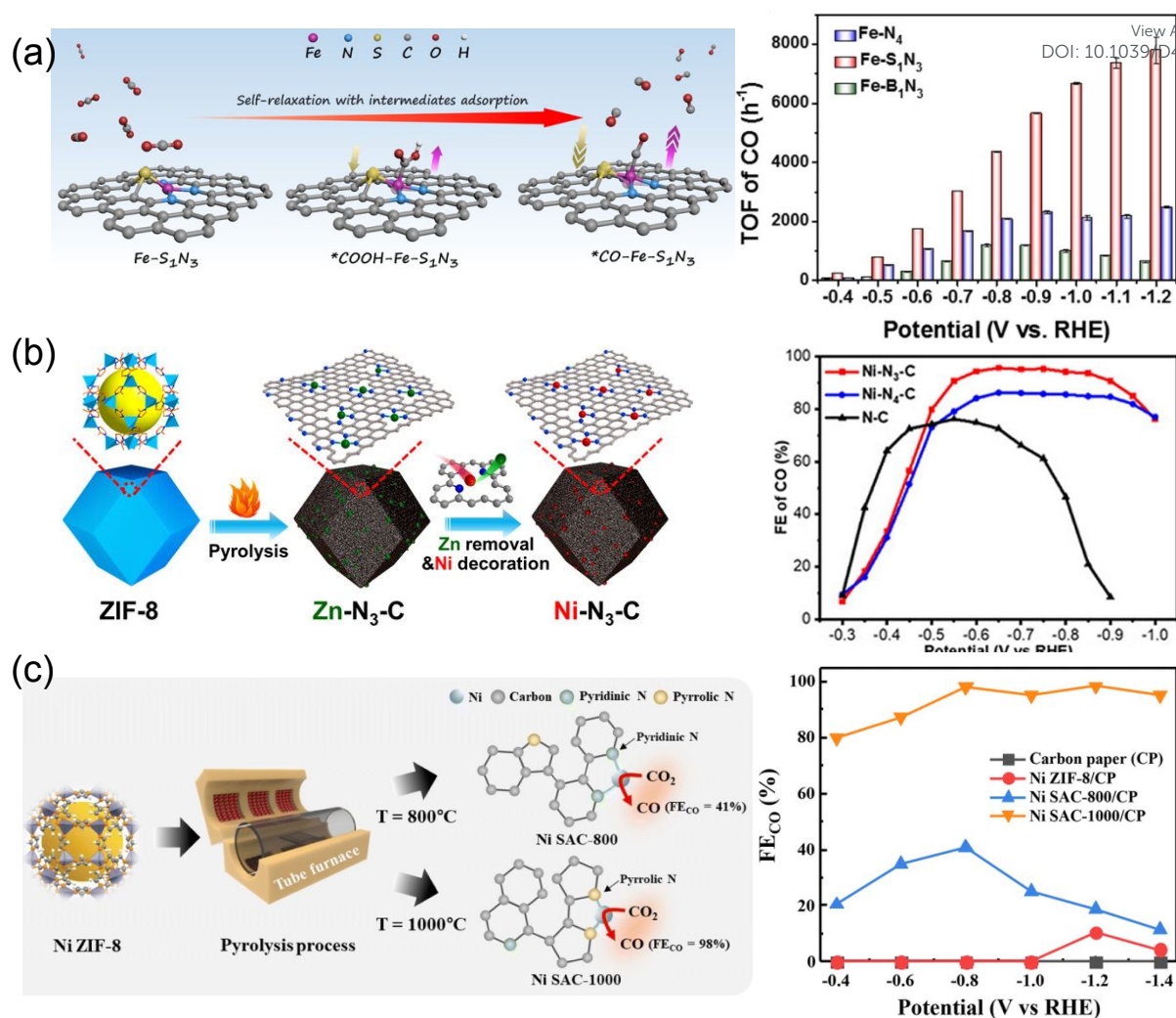**Fig. 10** (a) Schematic illustration showcasing the structural distortion of the $Fe-S_1N_3$ site with adsorbed various intermediates[47]. Copyright 2023, Wiley-VCH. (b) Schematic illustration for the fabrication of low-coordination single-atom Ni electrocatalysts[48]. Copyright 2021, Wiley-VCH. (c) Schematic illustration for the fabrication of pyrrolic N-stabilized low-coordinated Ni SAC and $FE_{CO}$ at different potentials[98]. Copyright 2024, Royal Society of Chemistry

effect of Fe and Ni atom pairs, the $Fe_1-Ni_1$-N-C catalyst presented better selectivity for electrocatalytic reduction of $CO_2$ to CO than $Fe_1$-N-C and $Ni_1$-N-C catalysts. Theoretical simulations revealed that single Fe atoms can be highly activated by adjacent Ni via non-bonding interactions in $Fe_1-Ni_1$-N-C, significantly facilitating the formation of COOH* intermediate and thereby accelerating the overall $CO_2$ reduction. Similarly, a series of atomically dispersed and nitrogen coordinated dual-metal sites (ZIF-NC-Ni-Fe, ZIF-NC-Fe-Co, and ZIF-NC-Ni-Co) were designed **(Fig. 9b)**[95]. Among these, the ZIF-NC-Ni-Fe catalyst exhibited the most efficient $CO_2$RR activity, achieving a maximum $FE_{CO}$ of 97.8% at -0.6 V, surpassing ZIF-NC-Fe-Co ($FE_{CO}$ = 76.3%) and ZIF-NC-Ni-Co ($FE_{CO}$ = 68.9%). After characterization and theoretical prediction, it was confirmed that the most active N-coordinated dual-metal site was 2N-bridged $(Fe-Ni)N_6$, where $FeN_4$ and $NiN_4$ moieties were shared with two N atoms. The redistributed electrons on the Fe and Ni atoms in the ZIF-NC-Ni-Fe led to an optimal synergistic effect between the two metals, which facilitated

*COOH adsorption and *CO desorption kinetics while suppressing the HER. In another report, CuNi atomic cluster embedded Ni/Cu dual atomic sites catalyst (CuNiAC@Ni/Cu-N-C) was designed **(Fig. 9c)**[194]. The introduction of $Cu_3Ni$ atomic clusters into $N_4Ni/CuN_3$ dual sites enhanced the electronic conductivity and decreased the energy barrier. Therefore, CuNiAC@Ni/Cu-N-C showed excellent performance with a maximum $FE_{CO}$ of 98.2% at -0.7 V and kept a continuous electrocatalysis for 70 h.

#### 5.2.2 Nitrogen coordination environment engineering

The preceding section highlighted the significant role of metal centers, typically $M-N_4$, following structural transformation at high temperature. Apart from the ion reduction during the pyrolysis process, the coordination environment also fluctuates under various conditions, including temperature and atmosphere. Through a thermal treatment method involving dicyandiamide[86], the fabrication of structural $Fe-N_5$ units on defective porous carbon nanofibers ($Fe-N_5$/DPCF) was

prepared. The Fe-$N_5$/DPCF exhibited a maximal $FE_{CO}$ of 93.1%, ascribed to the enhanced electronic localization that facilitated the CO desorption and reduced the energy barrier for $CO_2RR$. Jin et al. also accomplished asymmetric coordination of Fe single-atom catalysts **(Fig. 10a)**[47], forming a Fe-$S_1N_3$ unit with three N atoms and one S atom. Compared with Fe-$N_4$ (91.53 %) and Fe-$B_1N_3$ (90.17 %), the catalyst with Fe-$S_1N_3$ active sites showed a maximum $FE_{CO}$ of 99.02 % at -0.5 V and a TOF of 7804.34 $h^{-1}$. Operando XAFS results combined with DFT calculations revealed that the larger geometric radius of S atoms resulted in geometric distortion in the Fe-$S_1N_3$ sites, triggering self-relaxation behavior during intermediate adsorption. Analogous instances, such as the Ga atom in a Ga-$N_3$S-PC configuration, have also been reported[83].

By manipulating pyrolysis temperatures, low-coordinated Ni-$N_x$ sites were synthesized by replacing the atomically dispersed Zn sites with Ni atoms in a post-synthetic metal substitution strategy **(Fig. 10b)**[48]. The prepared Ni-$N_3$-C catalyst showed excellent CO selectivity with an $FE_{CO}$ of 95.6 % and a TOF of 1425 $h^{-1}$ at -0.65 V, superior to the Ni-$N_4$-C catalyst. DFT calculations revealed that low-coordinated Ni-$N_3$-C active sites significantly enhanced COOH* formation, thereby promoting $CO_2$ conversion. By varying pyrolysis temperatures, significantly fewer low-coordinated Ni-$N_2$-C sites were synthesized through a host-guest cooperative protection strategy involving the introduction of polypyrrole into a bimetallic MOF (MgNi-MOF-74)[34]. The resulting catalyst, NiSA-$N_2$-C, displayed high $FE_{CO}$ (98%) and TOF (1622 $h^{-1}$), surpassing the performance of NiSA-$N_3$-C and NiSA-$N_4$-C. Coordination environment, which encompasses not only the amounts but also the types of N atoms, played a crucial role in these disparities. Through the pyrolysis of Ni ZIF-8 within the temperature range of 800°C to 1000°C **(Fig. 10c)**, the ratio of pyrrolic N/pyridinic N increased from 0.37 to 1.01 as well as Ni-$N_x$ sites with decreased coordination number from 3.14 to 2.63[98]. The pyrrolic N-stabilized Ni SAC-1000 showed heightened activity with an $FE_{CO}$ of 98.24% at -0.8 V, surpassing the Ni SAC-800 with an $FE_{CO}$ of 40.76% at -0.8 V. DFT calculations revealed that the synergistic effect of the pyrrolic N and low-coordinated Ni could decreased the desorption energy barrier of *CO during the $CO_2RR$, promoting the conversion of $CO_2$ to CO.

### 5.2.3 Other heteroatom coordination environment engineering

In addition to N atoms, the coordination of single-atom catalysts with other heteroatoms also significantly influences the electrocatalytic performance, recognized as significant contributors to tuning of MOF-derived electrocatalysts. In fact, the coordination environment of other heteroatoms (such as O, P, S, Cl, etc.) including the quantity and types have also been reported to significantly influence the electrocatalytic performance of $CO_2RR$[195].

The recent literature has brought attention to the often-overlooked O atoms. Zhang et al. [58] reported an O-coordinated Fe$N_4$ active site (Fe$N_4$-O) through the pyrolysis of an O- and N-rich MOF (Fe-IRMOF-3) as shown in **Fig. 11a**. The atomically dispersed Fe$N_4$-O active sites broke the symmetrical structure

of Fe-$N_4$ sites and exhibited a superior catalytic performance compared to Fe$N_4$, reaching an $FE_{CO}$ of 95% at 0.50 V and showing an excellent stability over 30 h. The enhanced performance was attributed to the axial O coordination, which not only regulated the binding energy of intermediates and shifted the d-band center of Fe-3d orbits, facilitating CO desorption, but also inhibited the competitive hydrogen production. A similar modulation of asymmetric atomic interface was also observed in Cu single-atom catalysts prepared by pyrolyzing Cu-Zn/MOF-74[92]. The catalyst with CuN$_3$O/C active sites delivered a higher $FE_{CO}$ of 96% at -0.8 V compared to CuCO$_3$/C ($FE_{CO}$ of 20.0% at -0.5 V) and a higher TOF up to 2782.6 $h^{-1}$. DFT calculations revealed that the incorporation of N and O atoms in CuN$_3$O/C helped regulate the asymmetric atomic interface, leading to reduction in the Gibbs free energy of CO* desorption and ultimately improved catalytic performance.

S atoms, possessing lower electronegativity to N atoms can also alter the electronic structure through the formation of M-S bonds. Yang et al.[90] synthesized a S/N co-coordinated Ni single-atom catalyst (Ni-SNC) by pyrolysis of a SO$_4^{2-}$ doped Zn/Ni ZIF. The Ni atom interacted with 3 N atoms and a S atom to form an unsaturated Ni-$N_3$-S active site. The unsaturated Ni-$N_3$-S active site reduced the energy barrier of $CO_2 \rightarrow$ COOH* conversion in the $CO_2RR$ process and S further improved the current density. A similar approach involved the incorporation of S and N atoms into the atomically dispersed pyrrole-type Fe-$N_4$ through a series of "solvothermal-solvothermal-pyrolysis" treatment, featuring p-d orbital hybridization in the second coordination layer **(Fig. 11b)**[97]. The S-doped pyrrole-type Fe-$N_4$ electrocatalyst (S/Fe-po$N_4$-C) not only modulated the electron density of the Fe site, facilitating the desorption of *CO, but also compressed $H_2$ evolution. This catalyst exhibited outstanding performance, achieving an $FE_{CO}$ of 98% and TOF of 4621.2 $h^{-1}$. *In situ* characterizations and calculations indicated that the p-d orbital hybridization balanced the adsorption of *COOH and *CO, and accelerated the proton transfer.

P atoms also exhibit a lower electronegativity compared to N atoms, often enhancing the catalytic activity through alterations in the coordination environment and optimization of adsorption process[196, 197]. Reports have highlighted similar catalytic sites of Ni-$P_1N_3$ and Fe-P nanocrystals anchored in N-doped carbon polyhedrons[197, 198]. Recently, Hu et al.[103] constructed a three-dimensional ordered microporous structure with ZnN$_4$ sites embedded in P-functionalized carbon (H-3DOM-ZnN$_4$/P-C). The rich hollow walls exposed more active sites while P atoms could adjust the electronic structure of ZnN$_4$ sites, optimizing the adsorption of *COOH intermediates. The H-3DOM-ZnN$_4$/P-C showed approximately 100% $FE_{CO}$ at -0.6 V and a high TOF up to 7.8×10$^4$ $h^{-1}$ at -1.0 V. Subsequently, they reported a $CO_2RR$ electrocatalyst with S and P co-doped, donated as ZnN$_4$S$_1$/P-HC, employing a "synergistically near- and
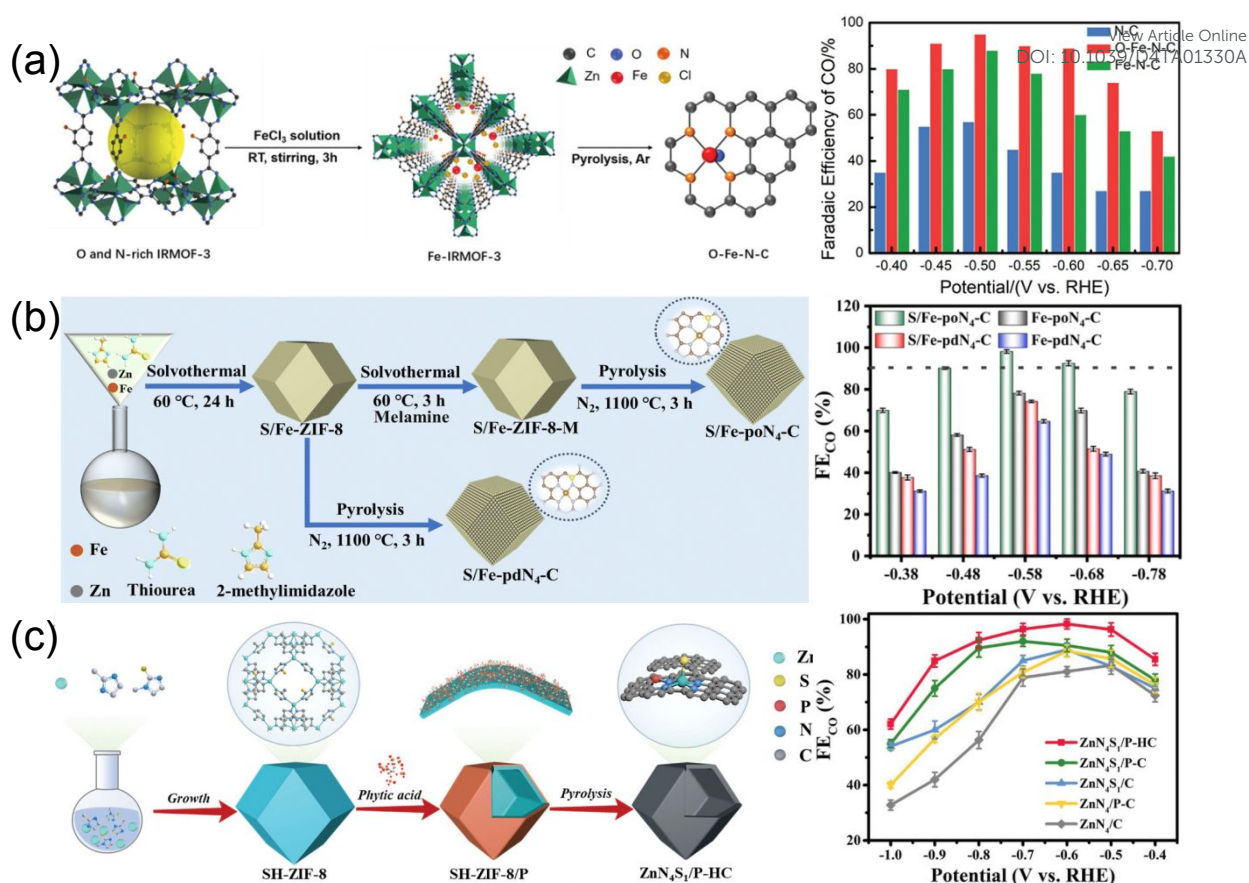
**Fig. 11** (a) Schematic synthesis of O-Fe-N-C and $FE_{CO}$ in $CO_2$-saturated 0.5 M $KHCO_3$. Copyright 2022, Wiley-VCH[58]. (b) Schematic illustration of preparing S/Fe-poN$_4$-C. Copyright 2024, Royal Society of Chemistry[97]. (c) Schematic illustration of the synthesis of ZnN$_4$S$_1$/P-HC. Copyright 2023, Wiley-VCH[104].

long-range regulation" strategy (**Fig. 11c**)[104]. The Zn-N$_4$ was decorated with axial S ligand in the first coordination and adjacent P atom in the second coordination, leading to the enhancement of charge density in Zn sites. The optimization improved the adsorption of *COOH intermediates, resulting in exceptional performance with $FE_{CO}$ close to 100% at -0.6 V.

## 6. Stability and reconstruction issues

As $CO_2RR$ is usually performed under various reduction potentials, which may lead to the reduction of metal ions of MOFs under certain circumstances. For example, bismuth (Bi) based electrocatalysts, are considered environmentally friendly for producing formates due to the low toxicity and inert HER activity[199-201]. Lamagni et al.[56] reported that Bi(1,3,5-tris(4-carboxyphenyl)benzene) MOF, donated as Bi(btb), underwent an *in situ* structural rearrangement under $CO_2RR$ conditions, forming well-dispersed and highly active Bi nanoparticles for the $CO_2$ conversion (**Fig. 12a**). Interestingly, the inherent poor conductivity of Bi(btb) was overcome by the structural rearrangement. Following $CO_2RR$ testing, FE of formates reached 95% at an overpotential of 770 mV, with a mass activity of up to 261(13) A·g$^{-1}$ achieved. Cao et al.[118] prepared atomically thin bismuthene (Bi-ene) by *in situ* electrochemical

transformation of bismuth-based metal-organic layers (**Fig. 12b**). The as-obtained Bi-ene exhibited a high selectivity (~100% FE) for formates, good stability in a broad potential range exceeding 0.35 V and ultrahigh current densities over 300 mA cm$^{-2}$. Attenuated Total Reflection Fourier-transform infrared spectroscopy (ATR-FTIR) spectroscopy and DFT calculations indicated that formate was produced via the OCHO* intermediate, and the adsorbed $HCO_3^-$ was found to have key roles in $CO_2RR$. Yao et al.[112] investigated a Bi-MOF constructed by bismuth oxyiodide and $H_3BTC$ (Benzene-1,3,5-tricarboxylic acid), demonstrating that electrolyte and potential mediated the restructuring processes (**Fig. 12c**). The Bi-MOF transformation to $Bi_2O_2CO_3$ and subsequent reduction to Bi played a pivotal role in determining morphology, defects, composition, and valence states, leading to enhanced formate yields and partial current densities. The resulted Bi nanosheets showed a maximum $FE_{HCOO^-}$ of 92 % at -1.1 V and a partial current density of -15 mA·cm$^{-2}$ at -1.3 V. The presence of unsaturated Bi atoms facilitated *OCHO intermediates adsorption, contributing to improved reaction efficiency. Huang et al.[202] further studied the transformation process of the Bi-
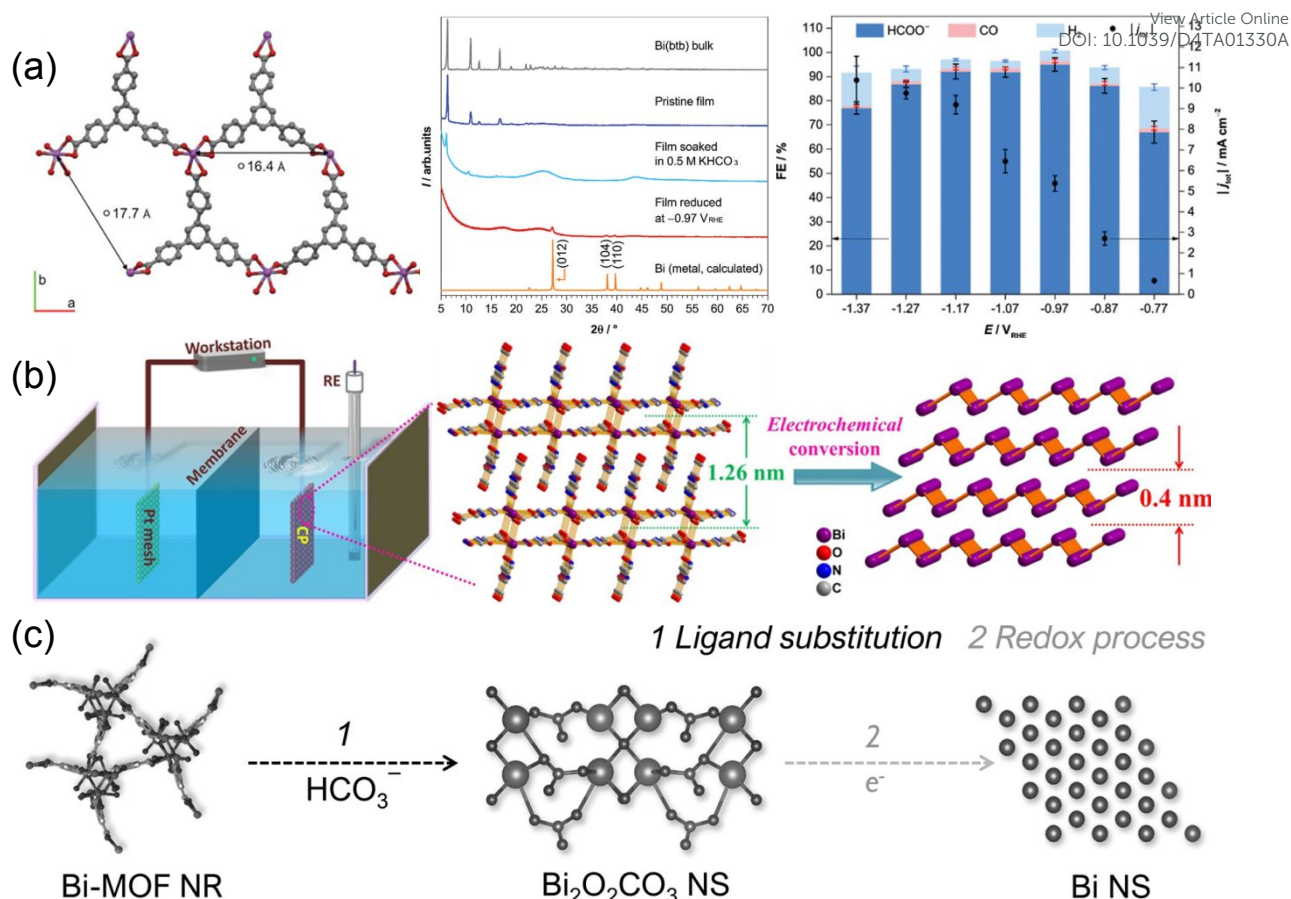
View Article Online
DOI: 10.1039/D4TA01330A

**Fig. 12** (a) Structural representation, XRD spectra and FE data of Bi(btb)[56]. Copyright 2020, Wiley-VCH. (b) Schematic illustration depicting the preparation of Bi-ene[118]. Copyright 2020, Wiley-VCH. (c) Schematic illustration depicting the *in situ* reconstruction process of Bi-MOF NR to Bi NS[112]. Copyright 2021, Wiley-VCH.

BTC (formed by Bi irons and $H_3BTC$) and its $CO_2RR$ performance. The transformation of the column Bi-BTC structure to nanosheets was influenced by the broken of Bi-O bond. And the exposed (020) crystal plane of restructured $Bi_2O_2CO_3$ favored *OCHO intermediate interactions. As a result, it achieved an FE of 96% and a current density of 25 mA·cm$^{-2}$. These studies underscored the significance of surface restructuring via electrochemical methods for developing high-performance and durable electrocatalysts.

Recently, the reconstruction of Cu-based MOFs was also investigated. Cu with low valence usually exhibits enhanced reactivity for $C_2$ products. Initially, utilizing an electrochemical conversion method (**Fig. 13a**), $CoS_2$ was obtained from a Co-ZIF-L precursor[203]. Subsequently, the $CoS_2$ template was converted into $Cu_2S$ nanocrystals through an electrochemical cation exchange process. The resulting $Cu_2S$ maintained their original three-dimensional morphology and a high density of grain boundaries. When applied in $CO_2RR$ process, the catalyst demonstrated notable efficiency in converting $CO_2$ to formates, achieving an impressive FE of 87.3%. Zhang et al.[204] reported a coordinatively unsaturated Cu paddle wheel (CU-CPW) clusters in defect-containing HKUST-1 (Cu(II)-BTC) prepared by atomized trimesic acid and $Cu(OH)_2$ strategy (**Fig. 13b**). $Cu_2(HCOO)_3$ in CU-

CPW is proven to be maintained after the electrochemical structural transformation and serve as the active sites. CU-CPW accelerated the PCET process compared with coordinatively saturated $Cu_2(HCOO)_4$, producing hydrocarbons from $CO_2$. Highly active and selective $C_2H_4$ electrocatalyst (CuPz$_2$-Act-30) derived from MOF CuPz$_2$ (Pz = Pyrazole) with dispersive $Cu/Cu_2O$ nanoclusters was prepared by *in situ* electrochemical reduction (**Fig. 13c**)[136]. It achieved a high FE of 70.2 ± 1.7% at -1.03 V toward $C_2H_4$ generation. *In situ* ATR-FTIR spectroscopy and DFT calculations indicated that the nanoclusters transformed by *in situ* reconstruction had a preference to adsorb local CO, promote C-C coupling and hydrogenation to produce $C_2H_4$. Moreover, restructuring multi-phase interfaces of $Ag/Cu/Cu_2OAg_{0.1}$/HKUST-1 in $Ag_{0.1}$/HKUST-1was achieved by 1 h electroreduction[133]. By leveraging the higher standard redox potential of Ag and its less negative formation enthalpy of oxides, Ag was expected to stabilize neighboring Cu(I). Tandem electrolysis was enabled by the weak bonding of Ag *CO to Cu(0)-Cu(I) sites. The derived electrocatalysts showed high FE of 57.2% at -1.3 V for $CO_2$ conversion to $C_2H_4$. Characterizations and calculations further highlighted the crucial role of Ag in stabilizing Cu(I) and increasing CO surface coverage, while the $Cu/Cu_2O$ interface reduced the energy
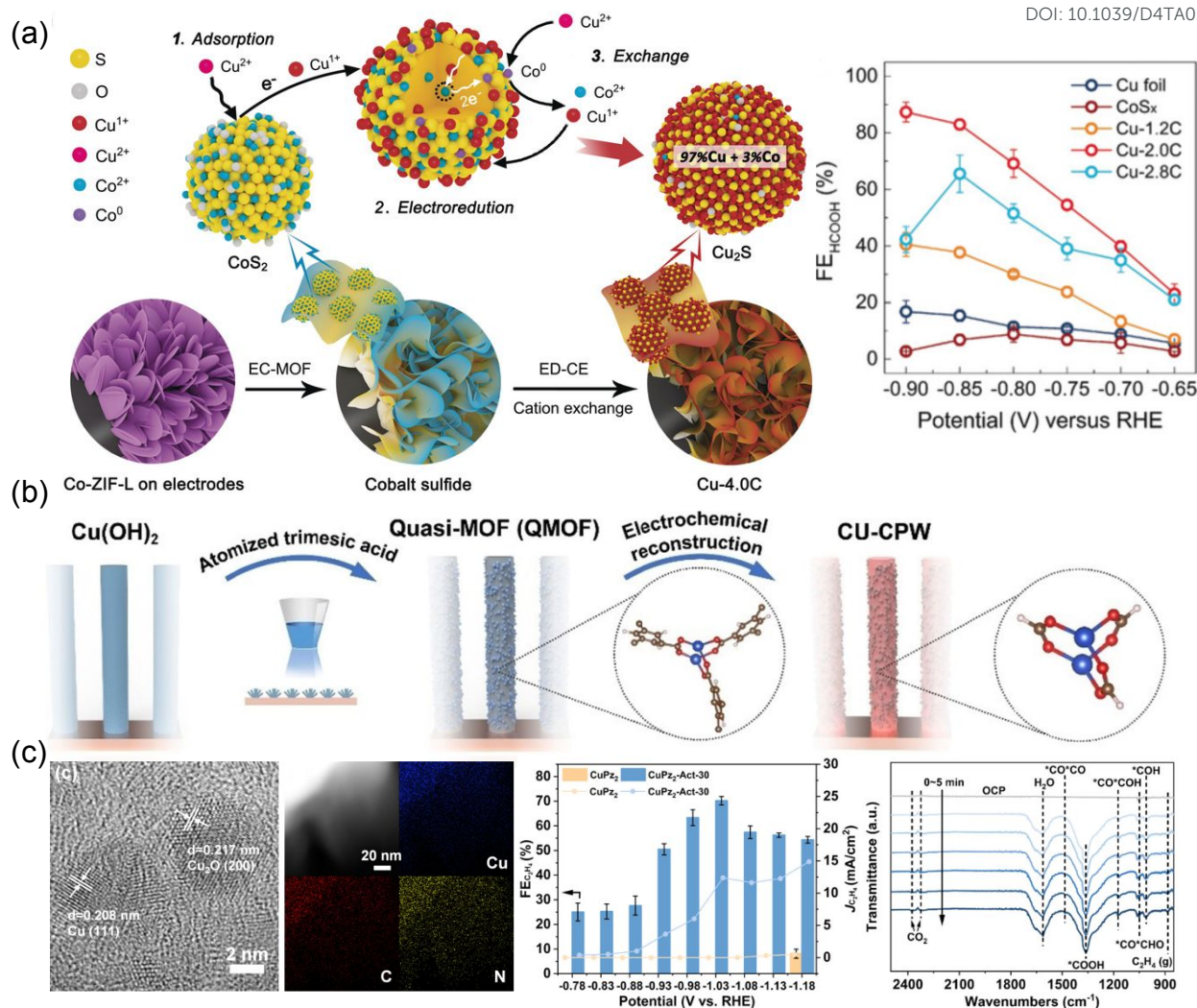
**Fig. 13** (a) Schematic illustration depicting the pathways/mechanisms for electrochemically driven cation exchange and FE of different catalysts[203]. Copyright 2020, Wiley-VCH. (b) Schematic illustration of the synthetic procedures for CU-CPW[204]. Copyright 2021, Wiley-VCH. (c) HRTEM images of CuPz$_2$-Act-30 with the corresponding elemental mapping, FE of C$_2$H$_4$, and *in situ* ATR-FTIR spectra of CuPz$_2$-Act-30[136]. Copyright 2022, American Chemical Society.

barrier of C-C coupling. Tandem electrolysis and electrochemical reduction were also successfully carried out on a [Cu$^I$(im)] (**1**) MOF (Im = imidazole)[129], resulting in the synthesis of CuN$_2$ and Cu$_2$N$_4$. The CuN$_2$/Cu(111) derivatives with Cu-N coordination exhibited superior performance compared to Cu$_2$N$_4$/Cu(111) with Cu-N and Cu-Cu coordination. The C$_{2+}$ products including C$_2$H$_4$, C$_2$H$_5$OH and n-C$_3$H$_7$OH were detected and the total FE$_{C2+}$ of CuN$_2$ reached 64.8%, surpassing the 43.9% efficiency of Cu$_2$N$_4$. This study emphasized the crucial role of pristine MOFs as catalysts for facilitating the conversion of CO$_2$ to CO.

## 7. Advanced Characterization Techniques

Though the well-defined structure of MOFs can be tailored to help understand the structure-activity relationship, the electrochemical stability of MOFs would be the major concern

for their application. Under the reduction conditions of CO$_2$RR, it is common for electrocatalysts undergoing reconstruction to build the new active sites[112, 136, 205, 206]. For example, Cu centers in Cu$_3$(HITP)$_2$ would be irretrievably reduced to Cu$^0$ under negative potential[135]. Cu clusters were detected during CO$_2$RR from Cu dimer in HKUST-1, and Cu/Cu$_x$S$_y$ interfaces was reconstructed from S-HKUST-1 (with Cu-S motif on HKUST-1) in CO$_2$RR conditions[71, 112, 134]. Therefore, it is important to monitor the structural changes of electrocatalysts during reactions to probe into the origin of CO$_2$RR on MOFs using *in situ* techniques. In addition, the dynamic electrode/electrolyte interfaces can be also monitored to shed light on the reaction mechanisms.

### 7.1 *In situ* XAS for probing active sites at atomic level

XAS has emerged as a popular technique to detect the local structure around single metal atoms, which is not limited to the
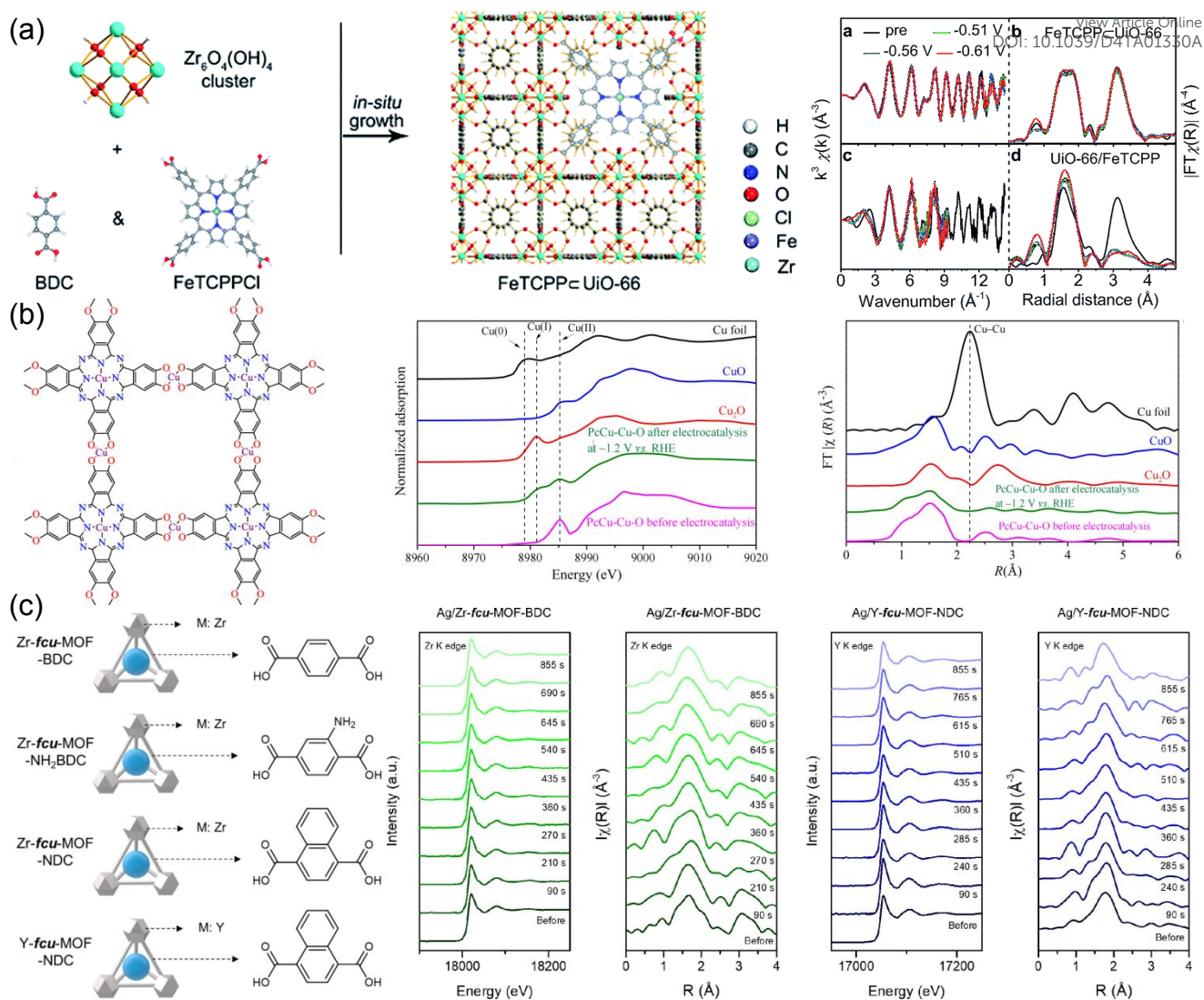
**Fig. 14** (a) Schematic of FeTCPP⊂UiO-66 MOF and Zr K-edge *in situ* EXAFS for the FeTCPP⊂UiO-66 and UiO-66/FeTCPP[102]. Copyright 2019, Royal Society of Chemistry. (b) Illustration of the structure, normalized Cu K-edge XANES and Fourier transform EXAFS of PcCu-Cu-O MOF[72]. Copyright 2021, American Chemical Society. (c) Schematic of the Zr-*fcu*-MOF-BDC, Zr-*fcu*-MOF-NH₂BDC, Zr-*fcu*-MOF-NDC and Y-*fcu*-MOF- NDC. *Operando* XAS analysis to the Zr K-edge XANES and EXAFS of Ag/Zr-*fcu*-MOF-BDC and the Y K-edge XANES and EXAFS of Ag/Y-*fcu*-MOF-NDC[87]. Copyright 2020, American Chemical Society.

state of samples under test. It can provide valuable information on the oxidation state, local coordination environment, and the electronic structure of the material[207]. The changes of metal nodes and the coordination environment surrounding the metal active centers can be reflected in the *in situ* XAS spectra to monitor the $CO_2RR$ dynamics at atomic level[208].

As shown in **Fig. 14a**, (5,10,15,20-tetrakis(4-carboxyphenyl)porphyrinato)-Fe(III) chloride (FeTCPPCl) was introduced into UiO-66 to form a robust active MOF (FeTCPP⊂UiO-66) with two carboxylic ligands[102]. The FeTCPP⊂UiO-66 realized nearly 100% selectivity for converting $CO_2$ to CO. *In situ* near edge XAS displayed almost unchanged curves at different potential compared to initial state, which demonstrated the structural stability of the FeTCPP⊂UiO-66 in electrochemical environment. However, the wavenumber of

the oscillation curve for UiO-66/FeTCPP (the physical mixture of FeTCPP and UiO-66) descended distinctly at -0.51 V, indicating its structural collapse. Due to the robust structure and protonation facilitator of the FeTCPP⊂UiO-66, the PCET pathway on the iron porphyrin sites was facilitated, leading to a low overpotential. Similarly, no significant changes in the *in situ* XAS spectra of the PcCu-Cu-O MOF catalyst confirmed its stability during $CO_2RR$ as shown in **Fig. 14b**[72]. The stability of Ag/Zr-*fcu*-MOF-BDC with Ag-incorporated was also investigated by *operando* XAS (**Fig. 14c**)[87]. The oxidation states, coordination number and atomic distance showed no observable difference during and after reaction as shown in the Zr K-edge X-ray absorption near edge structure (XANES) and extended X-ray absorption fine structure (EXAFS) spectra, indicating a constant Zr oxidation state and robust structure of Ag/Zr-*fcu*-MOF-BDC.

This was also found in the Y K-edge XANES and EXAFS spectra of Ag/Y-*fcu*-MOF-NDC, suggesting that the Zr- and Y-based MOFs with varying organic linkers and the metal nodes remained stable during $CO_2RR$.
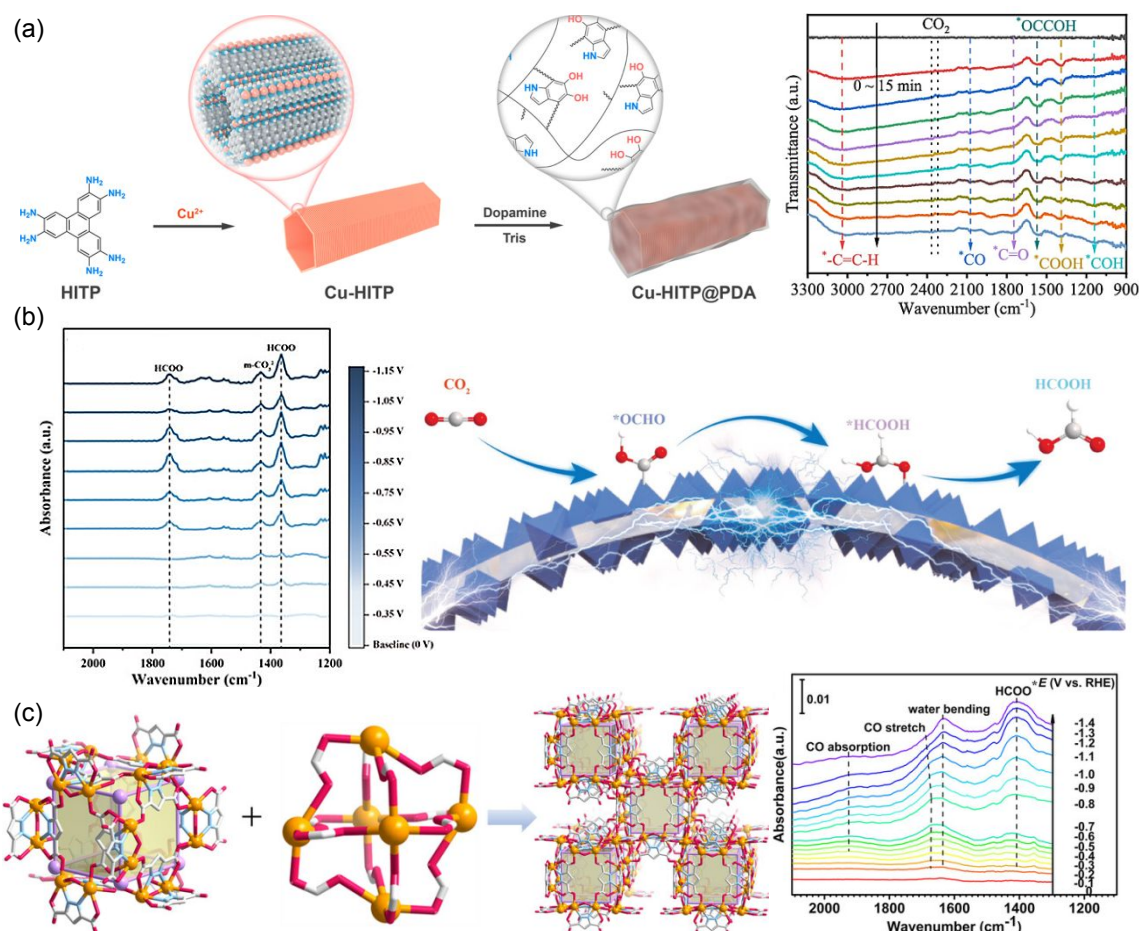


**Fig. 15** (a) Schematic of Cu-HITP@PDA and *in situ* FTIR spectra on Cu-HITP[131]. Copyright 2022, American Chemical Society. (b) *In situ* FTIR spectra of Cu@Bi$_{1/2}$ under various potentials and schematic diagram of $CO_2RR$[210]. Copyright 2023, Wiley-VCH. (c) Schematic of PZH-1 and *in situ* FTIR spectra for PZH-1[110]. Copyright 2023, Wiley-VCH.

## 7.2 *In situ* FTIR and Raman spectroscopy for monitoring dynamic interfaces

FTIR (Fourier-transform infrared spectroscopy) and Raman spectroscopy are useful spectroscopic techniques for capturing the reaction intermediates on the surface of catalysts and providing the information related to reaction products and pathways. By using the FTIR and Raman spectroscopy, the vibration modes of chemical bonds and formed structural coordination of the intermediates during the $CO_2RR$ can be acquired. However, the FTIR is usually interfered water absorption peak in aqueous solution, which is a great challenge to monitor intermediates when applied in aqueous solution. Instead of measuring the absorption of light like FTIR, Raman spectroscopy based on the scattering of light can compensate for this drawback due to the weak light scattering by water[209].

*In situ* FTIR spectroscopy was reported to capture the intermediates on the catalyst surface during $CO_2RR$. **Fig. 15a** shows the *in situ* FTIR spectra of Cu-HITP[131]. The bands at 1387 and 1400 $cm^{-1}$ were assigned to the *COOH and *COO, while the band at 2079 $cm^{-1}$ was assigned to the chemisorbed *CO. The absorption bands of the *CH$_2$ intermediate were also observed (3108 $cm^{-1}$ and 995 $cm^{-1}$). The band at 1150 $cm^{-1}$ was attributed to the *COH, indicating that the hydrogenation of *CO into a *COH. Additionally, the band at 1575 $cm^{-1}$ indicated the existence of *OCCOH, which meant *OCCOH was a key intermediate for $CO_2$ converting to C$_{2+}$ products. Similarly, a MOF-on-MOF (Cu@Bi$_{1/2}$, CAU-17 and ZJU-199) copper-based catalytic electrode was prepared by *in situ* synthesis on a foamed copper substrate[210] and studied using *in situ* FTIR to reveal the mechanism of HCOOH formation. As shown in **Fig. 15b**, the characteristic band located at 1363 $cm^{-1}$ corresponded to the HCOO$^-$ which displayed a trend of increasing and then decreasing with the potential from -0.35 to 0.95 V. In addition, there was a HCOO$^-$ band appeared at 1743 $cm^{-1}$ different from the Bi@Cu$_{1/2}$, indicating different reaction ways to generate

formic acid. The FE was further improved by a bismuth-based metal-organic frameworks (PZH-1), which was synthesized through a ligand-directing strategy using pyrazole-3,5-dicarboxylic acid (**Fig. 15c**)[110]. The bismuth-based ZMOF showed
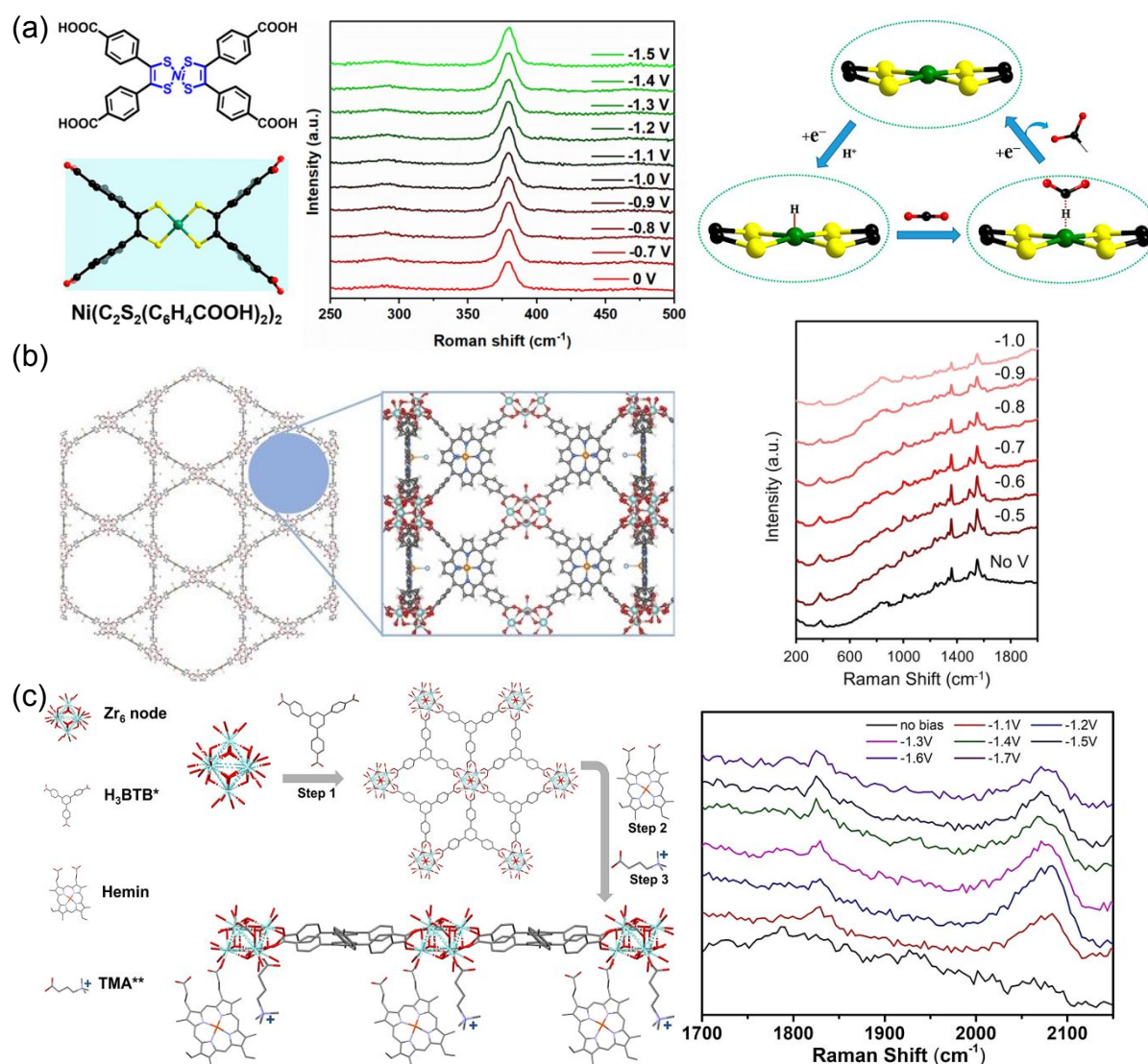
**Fig. 16** (a) Ligand structures of [Ni(C2S2(C6H4COOH)2)2], in situ Raman spectra of Ni-S bond in 1'' during the CO2RR process and proposed reaction paths for the formation of HCOO- on the [NiS4] sites107. Copyright 2021, American Chemical Society. (b) Immobilized metalloporphyrin in MOF and in situ Raman spectra for each potential for PCN-222(Fe)211. Copyright 2022, Wiley-VCH. (c) Schematic of Zr-BTB@Hemin-TMA, and in situ Raman spectra recorded at different potentials for Zr-BTB@Hemin-TMA82. Copyright 2022, Wiley-VCH.

ACO topological structure and strong coordination bonding within the Bi-based cages. *In situ* FTIR spectra of Bi-ZMOF showed characteristic band of two-oxygen bridged *HCOO (1414 cm$^{-1}$) at -0.4 V, which was intensified as the potential shifted from -0.4 V to -1.4 V. The band in the range of 1675-1685 cm$^{-1}$ associated with the C=O stretching mode became more prominent as the potential decreased. These findings indicated that the surface-bound Bi-*HCOO species played a crucial role as active intermediates for forming HCOOH.

The use of *in situ* Raman spectroscopy also provided valuable insights into the stability and reaction mechanisms of various electrocatalytic systems. Isomorphic MOF of $(Me_2NH_2^+)\{In^{III}-[Ni(C_2S_2(C_6H_4COO)_2)_2]\}\cdot3DMF\cdot1.5H_2O$ (**1''**, DMF = *N,N*-dimethylformamide) and $(Me_2NH_2^+)[In^{III}-(TTFTB)]\cdot0.7C_2H_5OH\cdot DMF$ (**2**, TTFTB = tetrathiafulvalene-tetrabenzoate) were used as electrocatalysts for CO$_2$RR[107]. [NiS$_4$] site in **1''** was considered to be the catalytic center and CO$_2$ binding site. Therefore, **1''** showed enhanced CO$_2$RR performance (FE$_{HCOO^-}$ = 89.6%) compared with **2** (FE$_{HCOO^-}$ =

54.7%). As shown in **Fig. 16a**, *in situ* Raman spectra exhibited no visible change in the $CO_2RR$ process, indicating the stability of the catalytic sites.

By immobilizing iron-porphyrin complexes into MOFs (**Fig. 16b**), PCN-222(Fe) exposed more active sites for $CO_2RR$ toward CO production, which showed an increasing current trend as the potential rising from -0.5 to -1.0 V[211]. *In situ* Raman spectra suggested that the structure was maintained under electrochemical bias. The characteristic bands of PCN-222(Fe) did not attenuate under electrochemical bias, indicating no structural reconstruction occurred during $CO_2RR$.

As shown in **Fig. 16c**, a cationic functional group (3-carboxypropyl)trimethylammonium) was immobilized to a Fe-porphyrin (Hemin)-modified Zr-BTB (termed Zr-BTB@Hemin-TMA) to enhance the activity and selectivity (~100%)[82]. *In situ* Raman spectroscopy conducted at different potentials suggested that two bands at 1840 $cm^{-1}$ and 2060 $cm^{-1}$ were attributed to catalyst-bounded CO stretching, indicating the presence of a weakly-bounded CO intermediate. The enhanced selectivity resulted from the electrostatic stabilization provided by the tethered functional group, which facilitated the swift release of CO as a product.

# 8. Challenges and Perspectives

## 8.1 Challenges

Metal-organic frameworks (MOFs), known for their orderly arrangement, extensive surface area, and adaptable structure, have been applied as electrocatalysts together with their derivatives for $CO_2$ reduction reactions ($CO_2RR$). Different metal centers and surrounding atoms yield distinct reduction products. By selecting appropriate metals and meticulously adjusting the coordination environment, desired reduced carbon products can be obtained. However, their application still faces many challenges due to inherent limitations such as poor conductivity, low chemical stability, and limited density of active sites. Some issues need to be considered in designing highly active and selective electrocatalysts, which we list as follow:

(1) The issue of poor conductivity arises from the organic ligands in MOFs, hindering electron transfer during the electrocatalytic reduction process. Despite of efforts in enhancing conductivity through strategies such as morphological and structural regulation of MOFs, creation of unsaturated metal coordination sites, incorporation of functionalized ligands and/or multi-metal components in MOFs, and integration into conductive active materials, the conductivity of two-dimensional (2D) MOFs remains inferior to that of 2D graphene. Improving the conductivity of MOFs is still an important research topic for future advancements in this field.

(2) MOFs bonded with coordination bond are prone to dissolution in the acidic or alkaline solution, underscoring the critical need to enhance the intrinsic stability of MOFs. Therefore, designing robust MOF catalysts adaptable to diverse environments is highly desirable. It may be considered to use

the strategies involve creating acid-resistant MOFs with high-valence state metals (hard acids) and carboxylate ligands (hard bases); developing alkali-resistant MOFs with low-valence state metals (soft acids) and azolate ligands (soft bases); improving the connectivity of building units; tightening or stiffening the ligands; and fortifying MOFs by substituting unstable building units with resilient counterparts for improving stability.

(3) The density of active sites within MOFs is crucial for assessing $CO_2RR$ performance. The active sites within MOFs typically encompass the metal centers and/or the surrounding ligands as illustrated in the above-mentioned sections, which have certain and thus limited quantities in a certain MOF structure. Therefore, enhancing the density of active sites in pristine MOFs is also effective to improve the $CO_2RR$ performance, which demands the exploration of newly designed MOFs. In addition, we also propose to incorporate functional guest molecules or elements into the pore channels of MOFs for enhancing the catalytic activity of MOFs toward $CO_2RR$, which may increase active sites in another way. Similarly, for the MOF derivatives, their active densities can be increased through impregnation methods or other approaches with optimized loading followed by high-temperature pyrolysis.

## 8.2 Perspectives

Aligned with these challenges and issues to be addressed in the application of MOFs and their derivatives for $CO_2RR$, the perspectives and future directions are proposed in this section. The metal nodes of MOFs or metal centers of MOF derivatives typically dictate the pathway toward various reduction products, while the coordinated organic ligands or the surrounding heteroatoms usually influence the selectivity by adjusting the electron density around the metal nodes or metal centers. Regulation of the metal oxidation state and surrounding coordination environment have been demonstrated to effectively affect the electrochemical performance. Despite of considerable efforts in applying MOFs and their derivatives for electrocatalytic $CO_2$ reduction, designing novel structures with high performance still remains challenging and desirable. Furthermore, mechanisms of existing MOFs and the derivatives need to be clearly studied to guide future structure design and performance improvement. In summary, we believe that future directions for designing and developing novel MOF-based catalysts can be focused on the following:

(1) Rationally designing of metal centers: The selection of appropriate metal centers is essential for achieving desired products. The $CO_2RR$ can be extended from single-metal MOF-based catalysts to bimetallic, trimetallic or polymetallic MOFs, which often exhibit enhanced performance due to the synergistic effects from the neighboring metal centers.

(2) Engineering of coordination environment: The microenvironment surrounding the metal centers significantly impacts product yield and selectivity. Modifying the ligands with coordination functional groups or introducing new functional coordinating ligands by direct synthesis or post-modification within MOFs may be used to improve electrocatalytic $CO_2RR$ performance.

**ARTICLE**

(3) Optimization of conductive substrates or inserted nanocomposites: Integrating conductive substrates or nanocomposites with MOFs can significantly decrease interfacial resistance, thereby improving electron transfer process. Consequently, suitable conductive substrates and/or nanocomposites may be developed for the future synthesis of conductive MOF-based catalysts.

(4) Advanced characterization techniques: Utilizing advanced characterization techniques provides an opportunity to unravel the intrinsic active sites and capture reaction intermediates, offering insight into the reaction mechanism. It is desired to further develop advanced *in situ* characterization techniques for monitoring the dynamic changes of the MOF-based electrocatalysts and electrode/electrolyte interfaces during the $CO_2RR$, thereby facilitating the design and synthesis of highly active and selective MOF-based electrocatalysts.

(5) Computational calculations: To support mechanistic studies, computational simulations such as DFT calculations and molecular dynamics are also needed from the view of thermodynamics and kinetics of $CO_2RR$. Machine learning may also be involved as an effective method for screening MOF-based catalysts[212]. The integration of computational tools will effectively pave the way for rational design of MOF-based catalysts in $CO_2RR$.

## Author Contributions

Xiaoming Liu: investigation, conceptualization, formal analysis, visualization, writing - original draft review and edit. Xuan-He Liu: supervision, funding acquisition, writing - review and edit. Xiangrui Zhang: writing - original draft review and edit. Huan Wang: supervision. Qinglan Zhao: supervision, funding acquisition, writing - review and edit.

## Conflicts of interest

The authors declare no conflicts of interest.

## Acknowledgements

## References

1.  X. Li, S. Wang, L. Li, Y. Sun and Y. Xie, *Journal of the American Chemical Society*, 2020, **142**, 9567-9581.
2.  C. Hu, S. Bai, L. Gao, S. Liang, J. Yang, S.-D. Cheng, S.-B. Mi and J. Qiu, *ACS Catalysis*, 2019, **9**, 11579-11588.
3.  H. Liu, Y. Zhu, J. Ma, Z. Zhang and W. Hu, *Advanced Functional Materials*, 2020, **30**, 1910534.
4.  Z. Liu, Z. Deng, G. He, H. Wang, X. Zhang, J. Lin, Y. Qi and X. Liang, *Nature Reviews Earth Environment*, 2022, **3**, 141-155.

5.  S. Bhattacharjee, M. Rahaman, V. Andrei, M. Miller, S. Rodríguez-Jiménez, E. Lam, C. Pornrungroj and E. Reisner, *Nature Synthesis*, 2023, **2**, 182-192.
6.  X. Chen, X. Su, H.-Y. Su, X. Liu, S. Miao, Y. Zhao, K. Sun, Y. Huang and T. Zhang, *ACS Catalysis*, 2017, **7**, 4613-4620.
7.  A. M. Appel, J. E. Bercaw, A. B. Bocarsly, H. Dobbek, D. L. DuBois, M. Dupuis, J. G. Ferry, E. Fujita, R. Hille and P. J. Kenis, *Chemical reviews*, 2013, **113**, 6621-6658.
8.  J. Shi, Y. Jiang, Z. Jiang, X. Wang, X. Wang, S. Zhang, P. Han and C. Yang, *Chemical Society Reviews*, 2015, **44**, 5981-6000.
9.  E. Le Saché and T. Reina, *Progress in Energy Combustion Science*, 2022, **89**, 100970.
10. D. He, J. Yan, K. Chen, L. Zhang, J. Lu, J. Liu and Y. Luo, *ACS Catalysis*, 2023, **13**, 12114-12124.
11. M. Li, Z. Sun and Y. H. Hu, *Chemical Engineering Journal*, 2022, **428**, 131222.
12. J. W. Ko, S.-W. Kim, J. Hong, J. Ryu, K. Kang and C. B. Park, *Green Chemistry*, 2012, **14**, 2391-2394.
13. E. W. Lees, B. A. Mowbray, F. G. Parlane and C. P. Berlinguette, *Nature Reviews Materials*, 2022, **7**, 55-64.
14. W. Xia, Y. Xie, S. Jia, S. Han, R. Qi, T. Chen, X. Xing, T. Yao, D. Zhou and X. Dong, *Journal of the American Chemical Society*, 2023, **145**, 17253-17264.
15. D. Song, Y. Lian, M. Wang, Y. Su, F. Lyu, Z. Deng and Y. Peng, *eScience*, 2023, **3**, 100097.
16. Z. Ma, T. Wan, D. Zhang, J. A. Yuwono, C. Tsounis, J. Jiang, Y.-H. Chou, X. Lu, P. V. Kumar and Y. H. Ng, *ACS Nano*, 2023, **17**, 2387-2398.
17. S. Yang, M. Jiang, W. Zhang, Y. Hu, J. Liang, Y. Wang, Z. Tie and Z. Jin, *Advanced Functional Materials*, 2023, **33**, 2301984.
18. P. Saha, S. Amanullah and A. Dey, *Accounts of Chemical Research*, 2022, **55**, 134-144.
19. S. Banerjee, C. S. Gerke and V. S. Thoi, *Accounts of Chemical Research*, 2022, **55**, 504-515.
20. G. Wen, B. Ren, Y. Zheng, M. Li, C. Silva, S. Song, Z. Zhang, H. Dou, L. Zhao and D. Luo, *Advanced Energy Materials*, 2022, **12**, 2103289.
21. S. Jin, Z. Hao, K. Zhang, Z. Yan and J. Chen, *Angewandte Chemie International Edition*, 2021, **60**, 20627-20648.
22. W. Lai, Y. Qiao, Y. Wang and H. Huang, *Advanced Materials*, 2023, **35**, 2306288.
23. X. Wang, Y. Jiang, K. Mao, W. Gong, D. Duan, J. Ma, Y. Zhong, J. Li, H. Liu and R. Long, *Journal of the American Chemical Society*, 2022, **144**, 22759-22766.
24. D. Sun, X. Xu, Y. Qin, S. P. Jiang and Z. Shao, *ChemSusChem*, 2020, **13**, 39-58.
25. Y. Kim, B. Kim, H. Choi, S. Kim, Y. Yun and J. Oh, *Chemical Engineering Journal*, 2023, **461**, 142126.
26. Z. Ma, C. Tsounis, C. Y. Toe, P. V. Kumar, B. Subhash, S. Xi, H. Y. Yang, S. Zhou, Z. Lin and K.-H. Wu, *ACS Catalysis*, 2022, **12**, 4792-4805.
27. L. Gao, S. Bai, Y. Zhang and C. Hu, *ChemCatChem*, 2022, **14**, e202200383.
28. Y. Yao, W. Zhuang, R. Li, K. Dong, Y. Luo, X. He, S. Sun, S. Al-Faifi, X. Sun and W. Hu, *Chemical Communications*, 2023, **59**, 9017-9028.

29. M. Zhang, M. Lu, M.-Y. Yang, J.-P. Liao, Y.-F. Liu, H.-J. Yan, J.-N. Chang, T.-Y. Yu, S.-L. Li and Y.-Q. Lan, *eScience*, 2023, **3**, 100116.

30. A. Xu, S.-F. Hung, A. Cao, Z. Wang, N. Karmodak, J. E. Huang, Y. Yan, A. Sedighian Rasouli, A. Ozden and F.-Y. Wu, *Nature Catalysis*, 2022, **5**, 1081-1088.

31. S. Liu, H. Tao, Q. Liu, Z. Xu, Q. Liu and J.-L. Luo, *ACS Catalysis*, 2018, **8**, 1469-1475.

32. R. Zhao, Y. Wang, G. Ji, J. Zhong, F. Zhang, M. Chen, S. Tong, P. Wang, Z. Wu and B. Han, *Advanced Materials*, 2023, **35**, 2205262.

33. T. Tang, Z. Wang and J. Guan, *Advanced Functional Materials*, 2022, **32**, 2111504.

34. Y. N. Gong, L. Jiao, Y. Qian, C. Y. Pan, L. Zheng, X. Cai, B. Liu, S. H. Yu and H. L. Jiang, *Angewandte Chemie International Edition*, 2020, **59**, 2705-2709.

35. Y. Zhou, R. Abazari, J. Chen, M. Tahir, A. Kumar, R. R. Ikreedeegh, E. Rani, H. Singh and A. M. Kirillov, *Coordination Chemistry Reviews*, 2022, **451**, 214264.

36. X. Liu, M. Zhuo, W. Zhang, M. Gao, X.-H. Liu, B. Sun and J. Wu, *Ultrasonics Sonochemistry*, 2020, **67**, 105179.

37. X.-H. Liu, W.-L. Hu, W.-J. Jiang, Y.-W. Yang, S. Niu, B. Sun, J. Wu and J.-S. Hu, *ACS Applied Materials & Interfaces*, 2017, **9**, 28473-28477.

38. R. Díaz, M. G. Orcajo, J. A. Botas, G. Calleja and J. Palma, *Materials letters*, 2012, **68**, 126-128.

39. Y. Yang and D. S. Sholl, *Journal of Materials Chemistry A*, 2022, **10**, 4242-4253.

40. K. Ren, X.-F. Guo, Y.-J. Tang, B.-H. Huang and H. Wang, *Analyst*, 2020, **145**, 7349-7356.

41. B. An, Z. Li, Y. Song, J. Zhang, L. Zeng, C. Wang and W. Lin, *Nature Catalysis*, 2019, **2**, 709-717.

42. B. Li, Z. Ju, M. Zhou, K. Su and D. Yuan, *Angewandte Chemie International Edition*, 2019, **58**, 7687-7691.

43. R. Chen, L. Cheng, J. Liu, Y. Wang, W. Ge, C. Xiao, H. Jiang, Y. Li and C. Li, *Small*, 2022, **18**, 2200720.

44. Y. Zhang, Q. Zhou, Z. F. Qiu, X. Y. Zhang, J. Q. Chen, Y. Zhao, F. Gong and W. Y. Sun, *Advanced Functional Materials*, 2022, **32**, 2203677.

45. M. Wen, N. Sun, L. Jiao, S. Q. Zang and H. L. Jiang, *Angewandte Chemie International Edition*, 2024, **63**, e202318338.

46. L. Jiao, J. Zhu, Y. Zhang, W. Yang, S. Zhou, A. Li, C. Xie, X. Zheng, W. Zhou and S.-H. Yu, *Journal of the American Chemical Society*, 2021, **143**, 19417-19424.

47. Z. Jin, D. Jiao, Y. Dong, L. Liu, J. Fan, M. Gong, X. Ma, Y. Wang, W. Zhang and L. Zhang, *Angewandte Chemie International Edition*, 2024, **63**, e202318246.

48. Y. Zhang, L. Jiao, W. Yang, C. Xie and H. L. Jiang, *Angewandte Chemie International Edition*, 2021, **60**, 7607-7611.

49. Y. Zhang, Y.-Y. Xing, C. Wang, R. Pang, W.-W. Ren, S. Wang, Z.-M. Li, L. Yang, W.-C. Tong and Q.-Y. Wang, *ACS Applied Materials Interfaces*, 2022, **14**, 23909-23915.

50. T. Zhao, H. Wu, X. Wen, J. Zhang, H. Tang, Y. Deng, S. Liao and X. Tian, *Coordination Chemistry Reviews*, 2022, **468**, 214642.

51. X. Wang, Z. Chen, X. Zhao, T. Yao, W. Chen, R. You, C. Zhao, G. Wu, J. Wang and W. Huang, *Angewandte Chemie International Edition*, 2018, **57**, 1944-1948.

52. Y. Zhang, Q. Zhou, Z. F. Qiu, X. Y. Zhang, J. Q. Chen, Y. Zhao, F. Gong and W. Y. Sun, *Advanced Functional Materials*, 2022, **32**, 2203677.

53. L. L. Zhuo, P. Chen, K. Zheng, X. W. Zhang, J. X. Wu, D. Y. Lin, S. Y. Liu, Z. S. Wang, J. Y. Liu and D. D. Zhou, *Angewandte Chemie International Edition*, 2022, **61**, e202204967.

54. R. Iqbal, M. B. Akbar, A. Ahmad, A. Hussain, N. Altaf, S. Ibraheem, G. Yasin, M. A. Khan, M. Tabish and A. Kumar, *Advanced Materials Interfaces*, 2022, **9**, 2101505.

55. Z. H. Zhu, Z. L. Liang, Z. H. Jiao, X. L. Jiang, Y. Xie, H. Xu and B. Zhao, *Angewandte Chemie International Edition*, 2022, **61**, e202214243.

56. P. Lamagni, M. Miola, J. Catalano, M. S. Hvid, M. A. H. Mamakhel, M. Christensen, M. R. Madsen, H. S. Jeppesen, X. M. Hu and K. Daasbjerg, *Advanced Functional Materials*, 2020, **30**, 1910408.

57. Q. Mo, S. Li, C. Chen, H. Song, Q. Gao and L. Zhang, *ACS Sustainable Chemistry Engineering*, 2024, **12**, 6093-6101.

58. T. Zhang, X. Han, H. Liu, M. Biset-Peiró, J. Li, X. Zhang, P. Tang, B. Yang, L. Zheng and J. R. Morante, *Advanced Functional Materials*, 2022, **32**, 2111446.

59. J. Li, G. Chen, Y. Zhu, Z. Liang, A. Pei, C.-L. Wu, H. Wang, H. R. Lee, K. Liu and S. Chu, *Nature Catalysis*, 2018, **1**, 592-600.

60. C. Genovese, M. E. Schuster, E. K. Gibson, D. Gianolio, V. Posligua, R. Grau-Crespo, G. Cibin, P. P. Wells, D. Garai and V. Solokha, *Nature communications*, 2018, **9**, 935.

61. A. R. Woldu, Z. Huang, P. Zhao, L. Hu and D. Astruc, *Coordination Chemistry Reviews*, 2022, **454**, 214340.

62. J. Yu, J. Wang, Y. Ma, J. Zhou, Y. Wang, P. Lu, J. Yin, R. Ye, Z. Zhu and Z. Fan, *Advanced Functional Materials*, 2021, **31**, 2102151.

63. K. P. Kuhl, E. R. Cave, D. N. Abram and T. F. Jaramillo, *Energy Environmental Science*, 2012, **5**, 7050-7059.

64. C. Qiu, K. Qian, J. Yu, M. Sun, S. Cao, J. Gao, R. Yu, L. Fang, Y. Yao and X. Lu, *Nano-Micro Letters*, 2022, **14**, 167.

65. X. Zhang, Y. Zhang, Q. Li, X. Zhou, Q. Li, J. Yi, Y. Liu and J. Zhang, *Journal of Materials Chemistry A*, 2020, **8**, 9776-9787.

66. J. D. Yi, D. H. Si, R. Xie, Q. Yin, M. D. Zhang, Q. Wu, G. L. Chai, Y. B. Huang and R. Cao, *Angewandte Chemie International Edition*, 2021, **133**, 17108-17114.

67. Y. Zhang, Q. Zhou, P. Wang, Y. Zhao, F. Gong and W. Y. Sun, *ChemSusChem*, 2022, **15**, e202102528.

68. Z. Tang, W. He, Y. Wang, Y. Wei, X. Yu, J. Xiong, X. Wang, X. Zhang, Z. Zhao and J. Liu, *Applied Catalysis B: Environmental*, 2022, **311**, 121371.

69. H.-L. Zhu, J.-R. Huang, X.-W. Zhang, C. Wang, N.-Y. Huang, P.-Q. Liao and X.-M. Chen, *ACS Catalysis*, 2021, **11**, 11786-11792.

70. W. Su, W. Guo and Y. Fan, *Chemical Engineering Journal*, 2023, **147**, 147204.

71. D. H. Nam, O. Shekhah, A. Ozden, C. McCallum, F. Li, X. Wang, Y. Lum, T. Lee, J. Li and J. Wicks, *Advanced Materials*, 2022, **34**, 2207088.

**ARTICLE**

Journal Name

72. X.-F. Qiu, H.-L. Zhu, J.-R. Huang, P.-Q. Liao and X.-M. Chen, *Journal of the American Chemical Society*, 2021, **143**, 7242-7246.

73. T. Yan, P. Wang and W. Y. Sun, *Small*, 2023, **19**, 2206070.

74. R. K. Aparna, V. Surendran, D. Roy, B. Pathak, M. M. Shaijumon and S. Mandal, *ACS Applied Energy Materials*, 2023, **6**, 4072-4078.

75. Y. Wang, B. J. Park, V. K. Paidi, R. Huang, Y. Lee, K.-J. Noh, K.-S. Lee and J. W. Han, *ACS Energy Letters*, 2022, **7**, 640-649.

76. X. Jiang, H. Li, J. Xiao, D. Gao, R. Si, F. Yang, Y. Li, G. Wang and X. Bao, *Nano Energy*, 2018, **52**, 345-350.

77. Z. Meng, J. Luo, W. Li and K. A. Mirica, *Journal of the American Chemical Society*, 2020, **142**, 21656-21669.

78. H. Zhong, M. Ghorbani-Asl, K. H. Ly, J. Zhang, J. Ge, M. Wang, Z. Liao, D. Makarov, E. Zschech and E. Brunner, *Nature communications*, 2020, **11**, 1409.

79. J. H. Cho, C. Lee, S. H. Hong, H. Y. Jang, S. Back, M. g. Seo, M. Lee, H. K. Min, Y. Choi and Y. J. Jang, *Advanced Materials*, 2023, **35**, 2208224.

80. T. Wen, M. Liu, S. Chen, Q. Li, Y. Du, T. Zhou, C. Ritchie and J. Zhang, *Small*, 2020, **16**, 1907669.

81. S. Dou, J. Song, S. Xi, Y. Du, J. Wang, Z. F. Huang, Z. J. Xu and X. Wang, *Angewandte Chemie International Edition*, 2019, **58**, 4041-4045.

82. R. Shimoni, Z. Shi, S. Binyamin, Y. Yang, I. Liberman, R. Ifraemov, S. Mukhopadhyay, L. Zhang and I. Hod, *Angewandte Chemie International Edition*, 2022, **61**, e202206085.

83. Z. Zhang, J. Zhu, S. Chen, W. Sun and D. Wang, *Angewandte Chemie International Edition*, 2023, **62**, e202215136.

84. H. Li, X. Liu, S. Chen, D. Yang, Q. Zhang, L. Song, H. Xiao, Q. Zhang, L. Gu and X. Wang, *Advanced Energy Materials*, 2019, **9**, 1900072.

85. F. Pan, H. Zhang, K. Liu, D. Cullen, K. More, M. Wang, Z. Feng, G. Wang, G. Wu and Y. Li, *ACS Catalysis*, 2018, **8**, 3116-3122.

86. Z. Li, J. Jiang, X. Liu, Z. Zhu, J. Wang, Q. He, Q. Kong, X. Niu, J. S. Chen and J. Wang, *Small*, 2022, **18**, 2203495.

87. D.-H. Nam, O. Shekhah, G. Lee, A. Mallick, H. Jiang, F. Li, B. Chen, J. Wicks, M. Eddaoudi and E. H. Sargent, *Journal of the American Chemical Society*, 2020, **142**, 21513-21521.

88. T. A. Al-Attas, N. N. Marei, X. Yong, N. G. Yasri, V. Thangadurai, G. Shimizu, S. Siahrostami and M. G. Kibria, *ACS Catalysis*, 2021, **11**, 7350-7357.

89. X. Wang, Z. Chen, X. Zhao, T. Yao, W. Chen, R. You, C. Zhao, G. Wu, J. Wang and W. Huang, *Angewandte Chemie International Edition*, 2018, **130**, 1962-1966.

90. X. Yang, J. Cheng, H. Lv, X. Yang, L. Ding, Y. Xu, K. Zhang, W. Sun and J. Zhou, *Chemical Engineering Journal*, 2022, **450**, 137950.

91. Y. Y. Liu, J. R. Huang, H. L. Zhu, P. Q. Liao and X. M. Chen, *Angewandte Chemie International Edition*, 2023, **62**, e202311265.

92. P. Song, B. Hu, D. Zhao, J. Fu, X. Su, W. Feng, K. Yu, S. Liu, J. Zhang and C. Chen, *ACS Nano*, 2023, **17**, 4619-4628.

93. Z. Xin, Y.-R. Wang, Y. Chen, W.-L. Li, L.-Z. Dong and Y.-Q. Lan, *Nano Energy*, 2020, **67**, 104233.

94. R. Yun, R. Xu, C. Shi, B. Zhang, T. Li, L. He, T. Sheng and Z. Chen, *Nano Research*, 2023, **16**, 1-7.

95. Y. Li, W. Shan, M. J. Zachman, M. Wang, S. Hwang, H. Tabassum, J. Yang, X. Yang, S. Karakalos and Z. Feng, *Angewandte Chemie International Edition*, 2022, **61**, e202205632.

96. R. Yun, F. Zhan, X. Wang, B. Zhang, T. Sheng, Z. Xin, J. Mao, S. Liu and B. Zheng, *Small*, 2021, **17**, 2006951.

97. Y. Yang, L. Chen, Z. Guo, S. Liu, P.-d. Wu, Z. Fang, K. Zhang and H. Li, *Journal of Materials Chemistry A*, 2024, **12**, 8991-9001.

98. J. W. Lim, D. H. Choo, J. H. Cho, J. Kim, W. S. Cho, O. F. N. Okello, K. Kim, S. Lee, J. Son and S.-Y. Choi, *Journal of Materials Chemistry A*, 2024, **12**, 11090-11100.

99. L. L. Ling, L. Jiao, X. Liu, Y. Dong, W. Yang, H. Zhang, B. Ye, J. Chen and H. L. Jiang, *Advanced Materials*, 2022, **34**, 2205933.

100. M. Feng, X. Wu, H. Cheng, Z. Fan, X. Li, F. Cui, S. Fan, Y. Dai, G. Lei and G. He, *Journal of Materials Chemistry A*, 2021, **9**, 23817-23827.

101. H. Cheng, X. Wu, M. Feng, X. Li, G. Lei, Z. Fan, D. Pan, F. Cui and G. He, *ACS Catalysis*, 2021, **11**, 12673-12681.

102. F. Mao, Y.-H. Jin, P. F. Liu, P. Yang, L. Zhang, L. Chen, X.-M. Cao, J. Gu and H. G. Yang, *Journal of Materials Chemistry A*, 2019, **7**, 23055-23063.

103. C. Hu, W. Yao, X. Yang, K. Shen, L. Chen and Y. Li, *Advanced Science*, 2024, **11**, 2306095.

104. C. Hu, Y. Zhang, A. Hu, Y. Wang, X. Wei, K. Shen, L. Chen and Y. Li, *Advanced Materials*, 2023, **35**, 2209298.

105. Y. Takaoka, J. T. Song, A. Takagaki, M. Watanabe and T. Ishihara, *Applied Catalysis B: Environmental*, 2023, **326**, 122400.

106. S.-Z. Hou, X.-D. Zhang, W.-W. Yuan, Y.-X. Li and Z.-Y. Gu, *Inorganic Chemistry*, 2020, **59**, 11298-11304.

107. Y. Zhou, S. Liu, Y. Gu, G.-H. Wen, J. Ma, J.-L. Zuo and M. Ding, *Journal of the American Chemical Society*, 2021, **143**, 14071-14076.

108. Z.-H. Zhao, J.-R. Huang, D.-S. Huang, H.-L. Zhu, P.-Q. Liao and X.-M. Chen, *Journal of the American Chemical Society*, 2024, **146**, 14349-14356.

109. Y. Yang, J. Huang, Y. Zou, Y. Li, T. Zhan, L. Huang, X. Ma, Z. Zhang and S. Xiang, *Applied Surface Science*, 2023, **618**, 156664.

110. Z. Jiang, M. Zhang, X. Chen, B. Wang, W. Fan, C. Yang, X. Yang, Z. Zhang, X. Yang and C. Li, *Angewandte Chemie International Edition*, 2023, **62**, e202311223.

111. R. Yang, Q. Huang, X. Sha, B. Gao and J. Peng, *International Journal of Molecular Sciences*, 2023, **24**, 13838.

112. D. Yao, C. Tang, A. Vasileff, X. Zhi, Y. Jiao and S. Z. Qiao, *Angewandte Chemie International Edition*, 2021, **60**, 18178-18184.

113. S. Ma, K. Wu, S. Fan, Y. Li, Q. Xie, J. Ma and L. Yang, *Separation and Purification Technology*, 2024, **339**, 126520.

114. Z. Gao, M. Hou, Y. Shi, L. Li, Q. Sun, S. Yang, Z. Jiang, W. Yang, Z. Zhang and W. Hu, *Chemical Science*, 2023, **14**, 6860-6866.

115. L. Mi, B. Chen, X. Xu, S. Cai, Y. He, Y. Wei, Y. Jiang, C. Zheng, S. Zhong and W. Hu, *Journal of Alloys and Compounds*, 2024, **978**, 173516.

116. Q. Huang, X. Sha, R. Yang, H. Li and J. Peng, *ACS Applied Materials Interfaces*, 2024, **16**, 13882-13892.

117.    Y. Zhang, S. Liu, N. Ji, L. Wei, Q. Liang, J. Li, Z. Tian, J. Su and Q. Chen, *Journal of Materials Chemistry A*, 2024, **12**, 7528-7535.

118.    C. Cao, D. D. Ma, J. F. Gu, X. Xie, G. Zeng, X. Li, S. G. Han, Q. L. Zhu, X. T. Wu and Q. Xu, *Angewandte Chemie International Edition*, 2020, **59**, 15014-15020.

119.    G. Liu, Q. T. Trinh, H. Wang, S. Wu, J. M. Arce-Ramos, M. B. Sullivan, M. Kraft, J. W. Ager, J. Zhang and R. Xu, *Small*, 2023, 2301379.

120.    Y.-Y. Liu, H.-L. Zhu, Z.-H. Zhao, N.-Y. Huang, P.-Q. Liao and X.-M. Chen, *ACS Catalysis*, 2022, **12**, 2749-2755.

121.    X. Tan, C. Yu, C. Zhao, H. Huang, X. Yao, X. Han, W. Guo, S. Cui, H. Huang and J. Qiu, *ACS Applied Materials & Interfaces*, 2019, **11**, 9904-9910.

122.    J. Lv, W. Li, J. Li, Z. Zhu, A. Dong, H. Lv, P. Li and B. Wang, *Angewandte Chemie International Edition*, 2023, **62**, e202217958.

123.    Y. L. Yang, Y. R. Wang, L. Z. Dong, Q. Li, L. Zhang, J. Zhou, S. N. Sun, H. M. Ding, Y. Chen and S. L. Li, *Advanced Materials*, 2022, **34**, 2206706.

124.    Y. Liu, S. Li, L. Dai, J. Li, J. Lv, Z. Zhu, A. Yin, P. Li and B. Wang, *Angewandte Chemie international Edition*, 2021, **60**, 16409-16415.

125.    Y. Zhang, X.-Y. Zhang and W.-Y. Sun, *ACS Catalysis*, 2023, **13**, 1545-1553.

126.    S. Chen, W. H. Li, W. Jiang, J. Yang, J. Zhu, L. Wang, H. Ou, Z. Zhuang, M. Chen and X. Sun, *Angewandte Chemie International Edition*, 2022, **61**, e202114450.

127.    P. Shao, W. Zhou, Q. L. Hong, L. Yi, L. Zheng, W. Wang, H. X. Zhang, H. Zhang and J. Zhang, *Angewandte chemie international edition*, 2021, **60**, 16687-16692.

128.    T. Yan, J.-H. Guo, Z.-Q. Liu and W.-Y. Sun, *ACS Applied Materials Interfaces*, 2021, **13**, 25937-25945.

129.    X.-D. Zhang, J.-M. Huang, X. Zhu, C. Liu, Y. Yin, J.-Y. Huang, Y. Li and Z.-Y. Gu, *Chinese Chemical Letters*, 2024, 109937.

130.    D.-S. Huang, H.-L. Zhu, Z.-H. Zhao, J.-R. Huang, P.-Q. Liao and X.-M. Chen, *ACS Catalysis*, 2022, **12**, 8444-8450.

131.    Z.-H. Zhao, H.-L. Zhu, J.-R. Huang, P.-Q. Liao and X.-M. Chen, *ACS Catalysis*, 2022, **12**, 7986-7993.

132.    J. Wang, J. Liu, Y. Song, S. Geng, Z. Peng, J. Yu, F. Liu, Y. Wang, S. Xi and Z. Zhang, *ACS Materials Letters*, 2023, **5**, 2121-2130.

133.    J. Feng, W. Zhang, D. Shi, Y. Jia, Y. Tang, Y. Meng and Q. Gao, *Chemical Science*, 2024.

134.    C. F. Wen, M. Zhou, P. F. Liu, Y. Liu, X. Wu, F. Mao, S. Dai, B. Xu, X. L. Wang and Z. Jiang, *Angewandte Chemie International Edition*, 2022, **61**, e202111700.

135.    H. Sun, L. Chen, L. Xiong, K. Feng, Y. Chen, X. Zhang, X. Yuan, B. Yang, Z. Deng and Y. Liu, *Nature Communications*, 2021, **12**, 6823.

136.    C. Liu, X.-D. Zhang, J.-M. Huang, M.-X. Guan, M. Xu and Z.-Y. Gu, *ACS Catalysis*, 2022, **12**, 15230-15240.

137.    M. Kempasiddaiah, R. Samanta, S. Panigrahi, R. K. Trivedi, B. Chakraborty and S. Barman, *Nanoscale*, 2024, **16**, 10458-10473.

138.    K. Zhao, Y. Liu, X. Quan, S. Chen and H. Yu, *ACS Applied Materials & Interfaces*, 2017, **9**, 5302-5311.

139.    X. Yang, J. Cheng, X. Yang, Y. Xu, W. Sun and J. J. C. E. J. Zhou, 2022, **431**, 134171.

140.    J. Liu, D. Yang, Y. Zhou, G. Zhang, G. Xing, Y. Liu, Y. Ma, O. Terasaki, S. Yang and L. Chen, *Angewandte Chemie International Edition*, 2021, **60**, 14473-14479.

141.    C. Hu, Z. Jiang, Q. Wu, S. Cao, Q. Li, C. Chen, L. Yuan, Y. Wang, W. Yang and J. Yang, *Nature Communications*, 2023, **14**, 4767.

142.    P. Lu, J. Lv, Y. Chen, Y. Ma, Y. Wang, W. Lyu, J. Yu, J. Zhou, J. Yin and Y. Xiong, *Nano Letters*, 2024, **24**, 1553-1562.

143.    S. Li, J. Yu, S. Zhang, W. Qiu, X. Tang, Z. Lin, R. Cai, Y. Fang, S. Yang and X. Cai, *Advanced Functional Materials*, 2024, **34**, 2311989.

144.    W. Su, W. Guo and Y. Fan, *Chemical Engineering Journal*, 2023, **477**, 147204.

145.    Z.-H. Zhao, J.-R. Huang, P.-Q. Liao and X.-M. Chen, *Journal of the American Chemical Society*, 2023, **149**, 26783-26790.

146.    J. Liu, Y. Wang, P. Mo, F. Yang, K. Jiang, Z. Cheng, Y. Liu, Z. Sun, Z. Liu and Y. Zhang, *Nano Research*, 2024, **17**, 3888-3894.

147.    Y. Zhang, K. Li, M. Chen, J. Wang, J. Liu and Y. Zhang, *ACS Applied Nano Materials*, 2019, **3**, 257-263.

148.    K. Zhao, X. Nie, H. Wang, S. Chen, X. Quan, H. Yu, W. Choi, G. Zhang, B. Kim and J. G. Chen, *Nature Communications*, 2020, **11**, 2455.

149.    S. Payra, S. Kanungo and S. Roy, *Nanoscale*, 2022, **14**, 13352-13361.

150.    Z.-H. Gao, K. Wei, T. Wu, J. Dong, D.-e. Jiang, S. Sun and L.-S. Wang, *Journal of the American Chemical Society*, 2022, **144**, 5258-5262.

151.    Y. Pan, R. Lin, Y. Chen, S. Liu, W. Zhu, X. Cao, W. Chen, K. Wu, W.-C. Cheong and Y. Wang, *Journal of the American Chemical Society*, 2018, **140**, 4218-4221.

152.    W. Xie, T. Yang, N. Tian, X.-H. Liu and J. Chen, *Energy & Fuels*, 2022, **36**, 958-964.

153.    H. Kim, D. Shin, W. Yang, D. H. Won, H.-S. Oh, M. W. Chung, D. Jeong, S. H. Kim, K. H. Chae and J. Y. Ryu, *Journal of the American Chemical Society*, 2021, **143**, 925-933.

154.    P. Wang, S. Meng, B. Zhang, M. He, P. Li, C. Yang, G. Li and Z. Li, *Journal of the American Chemical Society*, 2023, **145**, 26133-26143.

155.    R. Wang, J. Liu, L.-Z. Dong, J. Zhou, Q. Huang, Y.-R. Wang, J.-W. Shi and Y.-Q. Lan, *CCS Chemistry*, 2023, **5**, 2237-2250.

156.    Q. Lei, L. Huang, J. Yin, B. Davaasuren, Y. Yuan, X. Dong, Z.-P. Wu, X. Wang, K. X. Yao and X. Lu, *Nature Communications*, 2022, **13**, 4857.

157.    Z. Jiang, T. Wang, J. Pei, H. Shang, D. Zhou, H. Li, J. Dong, Y. Wang, R. Cao and Z. Zhuang, *Energy Environmental Science*, 2020, **13**, 2856-2863.

158.    Y. Zhao, L. Zheng, D. Jiang, W. Xia, X. Xu, Y. Yamauchi, J. Ge and J. Tang, *Small*, 2021, **17**, 2006590.

159.    C. Cui, Q. Cao, H. Jing, Z. Zhao, D. Wang, Y. J. S. Li and Interfaces, *Surfaces and Interfaces*, 2024, **48**, 104353.

160. X. Peng, L. Zeng, D. Wang, Z. Liu, Y. Li, Z. Li, B. Yang, L. Lei, L. Dai and Y. Hou, *Chemical Society Reviews*, 2023, **52**, 2193-2237.

161. B. Zhang, Y. Jiang, M. Gao, T. Ma, W. Sun and H. Pan, *Nano Energy*, 2021, **80**, 105504.

162. K. A. Adegoke and N. W. Maxakato, *Coordination Chemistry Reviews*, 2022, **457**, 214389.

163. H. Meng, Y. Han, C. Zhou, Q. Jiang, X. Shi, C. Zhan and R. Zhang, *Small Methods*, 2020, **4**, 2000396.

164. C. Li, L. Zhang, J. Chen, X. Li, J. Sun, J. Zhu, X. Wang and Y. Fu, *Nanoscale*, 2021, **13**, 485-509.

165. S. Mandal, S. Natarajan, P. Mani and A. Pankajakshan, *Advanced Functional Materials*, 2021, **31**, 2006291.

166. D.-W. Lim and H. Kitagawa, *Chemical Society Reviews*, 2021, **50**, 6349-6368.

167. J. Ye, J. Yan, Y. Peng, F. Li and J. Sun, *Catalysis Today*, 2023, **410**, 68-84.

168. M. Tang, H. Shen and Q. Sun, *The Journal of Physical Chemistry C*, 2019, **123**, 26460-26466.

169. Q. Cui, G. Qin, W. Wang, K. Geethalakshmi, A. Du and Q. Sun, *Applied Surface Science*, 2020, **500**, 143993.

170. Y. Tian, Y. Wang, L. Yan, J. Zhao and Z. Su, *Applied Surface Science*, 2019, **467**, 98-103.

171. G. Xing, L. Cheng, K. Li, Y. Gao, H. Tang, Y. Wang and Z. Wu, *New Journal of Chemistry*, 2020, **44**, 12299-12306.

172. Y. Tian, C. Zhu, L. Yan, J. Zhao and Z. Su, *Journal of Materials Chemistry A*, 2019, **7**, 15341-15346.

173. H. Zhong, M. Wang, G. Chen, R. Dong and X. Feng, *ACS Nano*, 2022, **16**, 1759-1780.

174. L. Majidi, A. Ahmadiparidari, N. Shan, S. N. Misal, K. Kumar, Z. Huang, S. Rastegar, Z. Hemmat, X. Zou and P. Zapol, *Advanced Materials*, 2021, **33**, 2004393.

175. J. Liu, D. Yang, Y. Zhou, G. Zhang, G. Xing, Y. Liu, Y. Ma, O. Terasaki, S. Yang and L. Chen, *Angewandte Chemie International Edition*, 2021, **60**, 14473-14479.

176. L. Huang, Z. Liu, G. Gao, C. Chen, Y. Xue, J. Zhao, Q. Lei, M. Jin, C. Zhu and Y. Han, *Journal of the American Chemical Society*, 2023, **145**, 26444-26451.

177. M. G. Lee, S. Kandambeth, X.-Y. Li, O. Shekhah, A. Ozden, J. Wicks, P. Ou, S. Wang, R. Dorakhan and S. Park, *Journal of the American Chemical Society*, 2024, **146**, 14267-14277.

178. Z.-Z. Wu, F.-Y. Gao and M.-R. Gao, *Energy Environmental Science*, 2021, **14**, 1121-1139.

179. Q. Fan, X. Zhang, X. Ge, L. Bai, D. He, Y. Qu, C. Kong, J. Bi, D. Ding and Y. Cao, *Advanced Energy Materials*, 2021, **11**, 2101424.

180. S. Li, A. V. Nagarajan, Y. Li, D. R. Kauffman, G. Mpourmpakis and R. Jin, *Nanoscale*, 2021, **13**, 2333-2337.

181. X.-L. Lv, L. Feng, L.-H. Xie, T. He, W. Wu, K.-Y. Wang, G. Si, B. Wang, J.-R. Li and H.-C. Zhou, *Journal of the American Chemical Society*, 2021, **143**, 2784-2791.

182. X. Cheng, J. Zhang, X. Tan, L. Zheng, D. Tan, L. Liu, G. Chen, Q. Wan, B. Zhang and F. Zhang, *Chemical Communications*, 2020, **56**, 7637-7640.

183. X. Mao, W. Gong, Y. Fu, J. Li, X. Wang, A. P. O'Mullane, Y. Xiong and A. Du, *Journal of the American Chemical Society*, 2023, **145**, 21442-21453.

184. A. K. Singh, L. Gu, A. Dutta Chowdhury and A. Indra, *Inorganic Chemistry*, 2023, **62**, 8803-8811.

185. T. Al-Attas, S. K. Nabil, A. S. Zeraati, H. S. Shiran, T. Alkayyali, M. Zargartalebi, T. Tran, N. N. Marei, M. A. Al Bari and H. Lin, *ACS Energy Letters*, 2022, **8**, 107-115.

186. A. Bencini and V. Lippolis, *Coordination Chemistry Reviews*, 2010, **254**, 2096-2180.

187. J. Wang, X. Huang, S. Xi, H. Xu and X. Wang, *Angewandte Chemie International Edition*, 2020, **59**, 19162-19167.

188. X. Xie, X. Zhang, M. Xie, L. Xiong, H. Sun, Y. Lu, Q. Mu, M. H. Rummeli, J. Xu, S. Li, J. Zhong, Z. Deng, B. Ma, T. Cheng, W. A. Goddard and Y. Peng, *Nature Communications*, 2022, **13**.

189. Z. Xin, J. Liu, X. Wang, K. Shen, Z. Yuan, Y. Chen and Y.-Q. Lan, *ACS Applied Materials Interfaces*, 2021, **13**, 54959-54966.

190. J. Deng, L. Qiu, M. Xin, W. He, W. Zhao, J. Dong and G. Xu, *Small*, 2024, 2311060.

191. C. Jia, Y. Zhao, S. Song, Q. Sun, Q. Meyer, S. Liu, Y. Shen and C. Zhao, *Advanced Energy Materials*, 2023, **13**, 2302007.

192. P. Su, K. Iwase, S. Nakanishi, K. Hashimoto and K. Kamiya, *Small*, 2016, **12**, 6083-6089.

193. C.-Y. Yuan, L. Feng, X.-T. Qin, J.-X. Liu, X. Li, X.-C. Sun, X.-X. Chang, B.-J. Xu, W.-X. Li and D. Ma, *Angewandte Chemie International Edition*, 2024, e202405255.

194. F. Chang, K. Zhu, C. Liu, J. Wei, S. Yang, Q. Zhang, L. Yang, X. Wang and Z. Bai, *Advanced Functional Materials*, 2024, 2400893.

195. Z. Qi, Y. Zhou, R. Guan, Y. Fu and J. B. Baek, *Advanced Materials*, 2023, **35**, 2210575.

196. B. Pan, X. Zhu, Y. Wu, T. Liu, X. Bi, K. Feng, N. Han, J. Zhong, J. Lu and Y. Li, *Advanced Science*, 2020, **7**, 2001002.

197. M. Qu, Z. Chen, Z. Sun, D. Zhou, W. Xu, H. Tang, H. Gu, T. Liang, P. Hu and G. J. N. R. Li, *Nano Research*, 2023, **16**, 2170-2176.

198. S. Liu, L. Wang, H. Yang, S. Gao, Y. Liu, S. Zhang, Y. Chen, X. Liu and J. Luo, *Small*, 2022, **18**, 2104965.

199. X. Zhang, X. Sun, S.-X. Guo, A. M. Bond and J. Zhang, *Energy Environmental Science*, 2019, **12**, 1334-1340.

200. N. Han, Y. Wang, H. Yang, J. Deng, J. Wu, Y. Li and Y. Li, *Nature Communications*, 2018, **9**, 1320.

201. J. P. Jones, G. S. Prakash and G. A. Olah, *Israel Journal of Chemistry*, 2014, **54**, 1451-1466.

202. Q. Huang, X. Sha, R. Yang, H. Li and J. Peng, *ACS Applied Materials & Interfaces*, 2024, **16**, 13882-13892.

203. W. He, I. Liberman, I. Rozenberg, R. Ifraemov and I. Hod, *Angewandte Chemie international Edition*, 2020, **59**, 8262-8269.

204. W. Zhang, C. Huang, J. Zhu, Q. Zhou, R. Yu, Y. Wang, P. An, J. Zhang, M. Qiu and L. Zhou, *Angewandte Chemie International Edition*, 2022, **61**, e202112116.

205. W. Zhang, Y. Yang, Y. Tang and Q. Gao, *Journal of Energy Chemistry*, 2022, **70**, 414-436.

206. P. Liu, P. Jing, X. Xu, B. Liu and J. Zhang, *ACS Applied Energy Materials*, 2021, **4**, 12128-12136.

207. C. Bressler and M. Chergui, *Chemical reviews*, 2004, **104**, 1781-1812.

208. K. Adarsh, N. Chandrasekaran and V. Chakrapani, *Frontiers in chemistry*, 2020, **8**, 137.

209.   C. Farber, J. Li, E. Hager, R. Chemelewski, J. Mullet, A. Y. Rogachev and D. Kurouski, *ACS Omega*, 2019, **4**, 3700-3707.
210.   S. Liu, L. Song, R. Liu, L. Li, D. Yang, S. Yuan and X. Dai, *Small*, 2023, **19**, 2304808.

211.   M. R. Smith, C. B. Martin, S. Arumuganainar, A. Gilman, B. E. Koel and M. L. Sarazen, *Angewandte Chemie International Edition*, 2023, **62**, e202218208.
212.   G. Hai, X. Xue, S. Feng, Y. Ma and X. Huang, *ACS Catalysis*, 2022, **12**, 15271-15281.

View Article Online
DOI: 10.1039/D4TA01770A

Journal of Materials Chemistry A Accepted Manuscript

Please do not adjust margins

## Data Availability Statements

All the data supporting this review have been cited from reported publications, which are indicated throughout this review with copyrights obtained.